Bioactive Materials 45 (2025) 479–495

Contents lists available at ScienceDirect

Bioactive Materials

journal homepage: www.keaipublishing.com/en/journals/bioactive-materials

3D-printed zinc oxide nanoparticles modified barium titanate/hydroxyapatite ultrasound-responsive piezoelectric ceramic composite scaffold for treating infected bone defects

Kai Chen [a,1], Fang Wang [b,1], Xiumei Sun [c], Wenwei Ge [d], Mingjun Zhang [a], Lin Wang [a], Haoyu Zheng [b], Shikang Zheng [a], Haoyu Tang [d], Zhengjie Zhou [b], Guomin Wu [a,*]

[a] Department of Oral, Plastic and Aesthetic Surgery, Hospital of Stomatology, Jilin University, Changchun, 130021, China
[b] Department of Pathogeny Biology, College of Basic Medical Sciences, Jilin University, Changchun, 130021, China
[c] Department of Orthodontics, Hospital of Stomatology, Jilin University, Changchun, 130021, China
[d] Key Laboratory of Automobile Materials of Ministry of Education, School of Materials Science and Engineering, Jilin University, Changchun, 130021, China

ARTICLE INFO

Keywords:
Piezoelectric ceramics
Zinc oxide nanoparticles
Antibacterial therapy
Bone regeneration
Low-intensity pulsed ultrasound

ABSTRACT

Clinically, infectious bone defects represent a significant threat, leading to osteonecrosis, severely compromising patient prognosis, and prolonging hospital stays. Thus, there is an urgent need to develop a bone graft substitute that combines broad-spectrum antibacterial efficacy and bone-inductive properties, providing an effective treatment option for infectious bone defects. In this study, the precision of digital light processing (DLP) 3D printing technology was utilized to construct a scaffold, incorporating zinc oxide nanoparticles (ZnO-NPs) modified barium titanate (BT) with hydroxyapatite (HA), resulting in a piezoelectric ceramic scaffold designed for the repair of infected bone defects. The results indicated that the addition of ZnO-NPs significantly improved the piezoelectric properties of BT, facilitating a higher HA content within the ceramic scaffold system, which is essential for bone regeneration. In vitro antibacterial assessments highlighted the scaffold's potent antibacterial capabilities. Moreover, combining the synergistic effects of low-intensity pulsed ultrasound (LIPUS) and piezoelectricity, results demonstrated that the scaffold promoted notable osteogenic and angiogenic potential, enhancing bone growth and repair. Furthermore, transcriptomics analysis results suggested that the early growth response-1 (EGR1) gene might be crucial in this process. This study introduces a novel method for constructing piezoelectric ceramic scaffolds exhibiting outstanding osteogenic, angiogenic, and antibacterial properties under the combined influence of LIPUS, offering a promising treatment strategy for infectious bone defects.

1. Introduction

The incidence of fracture-related infections following internal fixation is reported to range from 5 % to 20 %, while for open fractures, this rate increases to 30 % [1]. Infective bone defects present a severe threat, causing osteonecrosis, significantly compromising patient outcomes, increasing financial burdens, and prolonging hospital stays [2]. Unlike typical bone defects, infectious bone defects require implants that are not only robust in osteoinductive capabilities but also endowed with exceptional antibacterial properties [3]. Recently, numerous strategies have been developed to equip implants with antibacterial surfaces to reduce implant-associated infections [4]. Although these innovations offer numerous benefits, they suffer from limitations that obstruct their widespread clinical adoption. Consequently, there is a pressing need to develop an alternative bone graft material that merges broad-spectrum antimicrobial activity, unparalleled biocompatibility, and potent osteoinductive properties, thus providing an effective therapeutic solution for infectious bone defects.

Zinc oxide (ZnO), an amphoteric metal oxide, has attracted significant attention due to its potent and broad-spectrum antibacterial, antitumor, and low-toxicity characteristics, among which ZnO nanoparticles (ZnO-NPs) have received approval from the United States Food and Drug

Peer review under responsibility of KeAi Communications Co., Ltd.
* Corresponding author.
E-mail addresses: wugm@jlu.edu.cn, guominwu2006@sina.com (G. Wu).
[1] Kai Chen and Fang Wang are co-first authors.

https://doi.org/10.1016/j.bioactmat.2024.11.015
Received 25 July 2024; Received in revised form 22 October 2024; Accepted 10 November 2024

Administration's (USFDA) for clinical use, highlighted by their remarkable antibacterial efficacy [5–7]. Beyond their antimicrobial prowess, zinc, the second most abundant trace element in the human body, plays a crucial role in numerous physiological functions [8]. Approximately 30 % of the body's zinc is found in bone tissue, emphasizing its critical role in bone formation, development, mineralization, and maintenance [9]. Research has shown that the careful addition of ZnO-NPs to biomaterial surfaces promotes bone cell activity, triggering a cascade of favorable in vivo responses including adhesion, migration, proliferation, osteogenic differentiation, and mineralization [4,7,10]. Moreover, among various piezoelectric materials, ZnO is notable for its simple synthesis process and superior semiconductor properties, surpassing traditional piezoelectric ceramics and organic counterparts [11–13]. ZnO, a representative binary piezoelectric ceramic, is distinguished by its superior piezoelectric characteristics. These properties enable the development of various applications, including devices for power generation, water splitting, biomolecular detection, humidity regulation, and monitoring of pressure or strain, as well as photonics and gas detection applications [14]. Furthermore, as a beneficial additive, ZnO substantially enhances the electrical performance of lead-free piezoelectric ceramics [15–18].

Following the identification of piezoelectric characteristics in bone tissue, an array of piezoelectric substances has been utilized in the construction of scaffolds for bone tissue engineering. BT and polyvinylidene fluoride (PVDF) are among the most rigorously examined materials in this field [19–21]. Concurrently, novel piezoelectric materials have been synthesized to improve bone tissue restoration [22]. In this context, inorganic materials are recognized for their unique benefits and drawbacks in comparison to their organic, more flexible counterparts, with an overarching aim of enhancing osteogenic properties [23,24]. Extensive documentation supports that materials possessing robust piezoelectric traits not only expedite osteogenesis but also bolster the osteogenic differentiation of mesenchymal stem cells (MSCs) [25–27]. In recent decades, considerable advancements have been made in refining the composition of lead-free piezoelectric ceramics through the inclusion of dopants to achieve superior electrical characteristics [15,17,28–32]. ZnO, a prominent piezoelectric ceramic, has garnered significant interest for its capability to augment the electrical attributes of piezoelectric ceramics, thereby emerging as a preferred material among scholars.

Currently, LIPUS is a prevalent stimulation technique used to prompt piezoelectric materials to generate electrical energy. This ultrasound modality operates at frequencies of 1–3 MHz and features a significantly lower intensity ($<1W/cm^2$) than traditional ultrasound techniques. More than inducing electrical energy from piezoelectric materials, LIPUS has gained broad therapeutic use due to its biological effects, including thermal, mechanical, and cavitation influences. These effects initiate intracellular biochemical cascades that promote tissue repair and regeneration [33]. Recognized for its effectiveness, LIPUS was approved by the FDA in 1994 for treating fresh fractures and in 2000 for nonunions [34,35]. A recent extensive review highlights LIPUS's ability to accelerate bone formation in various contexts, such as fresh fractures, delayed unions, nonunions, and distraction osteogenesis, via complex molecular, biological, and biomechanical changes at the fracture site [36]. Beyond its use in fractures and nonunions, several randomized controlled trials have demonstrated LIPUS's efficacy in treating other conditions, including osteoarthritis [37] and root resorption [38]. Additionally, ongoing research reveals LIPUS's effects on the biological behavior of MSCs, affecting crucial aspects like viability, proliferation, migration, differentiation, and inflammatory responses [39–42]. This emphasizes LIPUS's broad therapeutic potential and highlights the need for further exploration of its extensive applications.

Our research team has previously demonstrated the commendable biosafety and osteogenic efficacy of piezoelectric ceramics composed of BT and HA [43]. However, two primary concerns have persisted: the relatively low proportion of HA incorporated and the inherent lack of antibacterial properties in the HA/BT ceramic system. To overcome these challenges, a study was initiated to incorporate ZnO-NPs into the BT matrix, aiming to enhance both the piezoelectric properties and the HA proportion in the composite while ensuring minimal disruption to the piezoelectric coefficient. Moreover, the addition of ZnO-NPs imparts a significant advantage by providing antibacterial capabilities to the piezoelectric ceramic system. This innovative approach not only addresses the limitations of the existing system but also opens new avenues for potential applications in biomedical and other fields where antibacterial properties are essential.

2. Results and discussion

2.1. Optimal ratio screening of ZnO-NPs, BT and HA

The fabrication of nZnO@BT/HA involved incorporating ZnO-NPs at various concentrations (ranging from 0 to 2.0 wt%) into the BT/HA matrix. The optimal concentration of ZnO-NPs was determined through a comprehensive assessment of antibacterial efficacy and cell viability across five distinct concentrations, aiming to balance optimal biocompatibility with robust antibacterial properties. Antibacterial assays indicated a marked antibacterial effect when ZnO-NP concentrations equaled or exceeded 1 wt% (Supplementary Fig. 1). Consequently, concentrations below 1 wt% were deemed suboptimal and excluded from further consideration. A CCK-8 assay was used to evaluate the toxicity profile of ZnO-NPs towards DPSCs (Supplementary Fig. 2). A significant decline in cell survival rate was observed at concentrations exceeding 1 wt%, whereas concentrations at or below 1 wt% showed no detrimental effects on DPSC viability. Therefore, the inclusion of 2 wt% ZnO-NPs was precluded from subsequent studies. Accordingly, 1 wt% ZnO-NPs was selected as the optimal concentration for further exploration, consistent with previous findings that emphasized the dose-dependent nature of ZnO-NPs' impact on cellular proliferation [44]. Specifically, low concentrations of ZnO-NPs have been found to stimulate cell growth, whereas high concentrations inhibit cell proliferation [45]. Our research aligns with these observations, revealing that as ZnO-NP concentration increases to 1 wt%, there is a proportional enhancement in cell proliferation ability. However, at 2 wt%, pronounced toxicity towards DPSCs becomes evident. Thus, to ensure optimal biocompatibility and cell proliferation potential, our study incorporated 1 wt% ZnO-NPs into the BT/HA system for further investigation. This decision is supported by the literature, optimizing the beneficial effects of ZnO-NPs while minimizing potential toxicity concerns [44,46].

Furthermore, prior research has highlighted the capability of ZnO-NPs to modulate the electrical characteristics of BT piezoelectric ceramics [47]. With this objective, 1 wt% ZnO-NPs was incorporated into various BT and HA compositions, ranging from 100:0 to 0:100 (x) BT/(100-x)HA (x = 100, 90, 80, 70, 60, 50, 0), to assess their effects on the piezoelectric and dielectric properties of the resultant BT/HA system. These hybrid systems were designated as ZnO@100BT, ZnO@90BT/10HA, ZnO@80BT/20HA, ZnO@70BT/30HA, ZnO@60BT/40HA, ZnO@50BT50/HA, and ZnO@100HA, reflecting varying proportions of BT and HA with 1 wt% ZnO-NPs. Analysis at 1 KHz and 37 °C (as detailed in Supplementary Fig. 3A), revealed that as the BT content decreased, the εr (relative permittivity) values also diminished, specifically: ZnO@100BT: 2329.4, ZnO@90BT/10HA: 729.6, ZnO@80BT/20HA: 310.4, ZnO@70BT/30HA: 95.0, ZnO@60BT/40HA: 33.8, ZnO@50BT50/HA: 28.6, and ZnO@100HA: 11.8. This pattern underscores the significant influence of BT content on the dielectric properties of the composite system. Supplementary Fig. 3B illustrates the piezoelectric coefficient (d_{33}) of the samples, showing a decline in d_{33} values with reduced BT content: ZnO@100BT: 83.83 pC/N, ZnO@90BT/10HA: 41.20 pC/N, ZnO@80BT/20HA: 8.61 pC/N, ZnO@70BT/30HA: 1.87 pC/N, ZnO@60BT/40HA: 0.63 pC/N, ZnO@50BT50/HA: 0.17 pC/N, and ZnO@100HA: 0 pC/N. Prior studies

have noted that the piezoelectric coefficient of bone tissue ranges from 0.7 to 2.3 pC/N [48]. Interestingly, the ZnO@70BT/30HA composition, with a d33 value of 1.87 pC/N, falls within this biological range, suggesting its potential for biocompatibility and functional mimicry with bone tissue. Consequently, this specific proportion has been chosen as the focal point for further research.

Upon comprehensive evaluation, 1 wt% ZnO-NPs was incorporated into a system with a 70/30 ratio of BT to HA, designated as ZnO@BT/HA for the experimental group. Additionally, systems composed solely of a 70/30 BT to HA ratio (BT/HA) and pure HA (HA) were selected as control groups for subsequent experimentation, ensuring a rigorous and comparative analysis.

2.2. Construction and characterization of ceramic simples

The structural characteristics of HA, BT/HA, and ZnO@BT/HA scaffolds were meticulously examined and compared (Fig. 1). The panoramic views of these scaffolds revealed distinctive color variations, with HA displaying a porcelain-like whiteness, while BT/HA and ZnO@BT/HA exhibited a warm tan hue (Fig. 1B). Fig. 1C details the post-sintering morphologies of these ceramic scaffolds, indicating that the integration of BT significantly alters the morphology of HA. Nonetheless, the microstructural integrity of BT/HA is largely maintained despite the incorporation of ZnO-NPs. Further elemental analysis included elemental mapping of Ca, P, Ti, Ba, and Zn (Fig. 1D) alongside the corresponding energy-dispersive X-ray (EDX) spectra (Fig. 1E), highlighting changes in surface elemental compositions among the scaffolds and confirming the successful integration of trace ZnO-NPs into the BT/HA system. The XRD patterns of HA, BT/HA, and ZnO@BT/HA scaffolds provide additional insights. As shown in Fig. 1F(1), the appearance of characteristic BT peaks in the BT/HA scaffold, absent in the HA scaffold, confirms the incorporation of BT. Notably, the ZnO@BT/HA scaffold shows no new characteristic peaks, indicating the absence of secondary phases [49]. In the refined XRD analysis [Fig. 1F (2)], the absence of secondary phases at all dopant concentrations confirms the successful incorporation of ZnO-NPs into BT, forming a solid solution without altering the primary phase structure. Results in Fig. 1G demonstrate that the average water contact angles of HA,

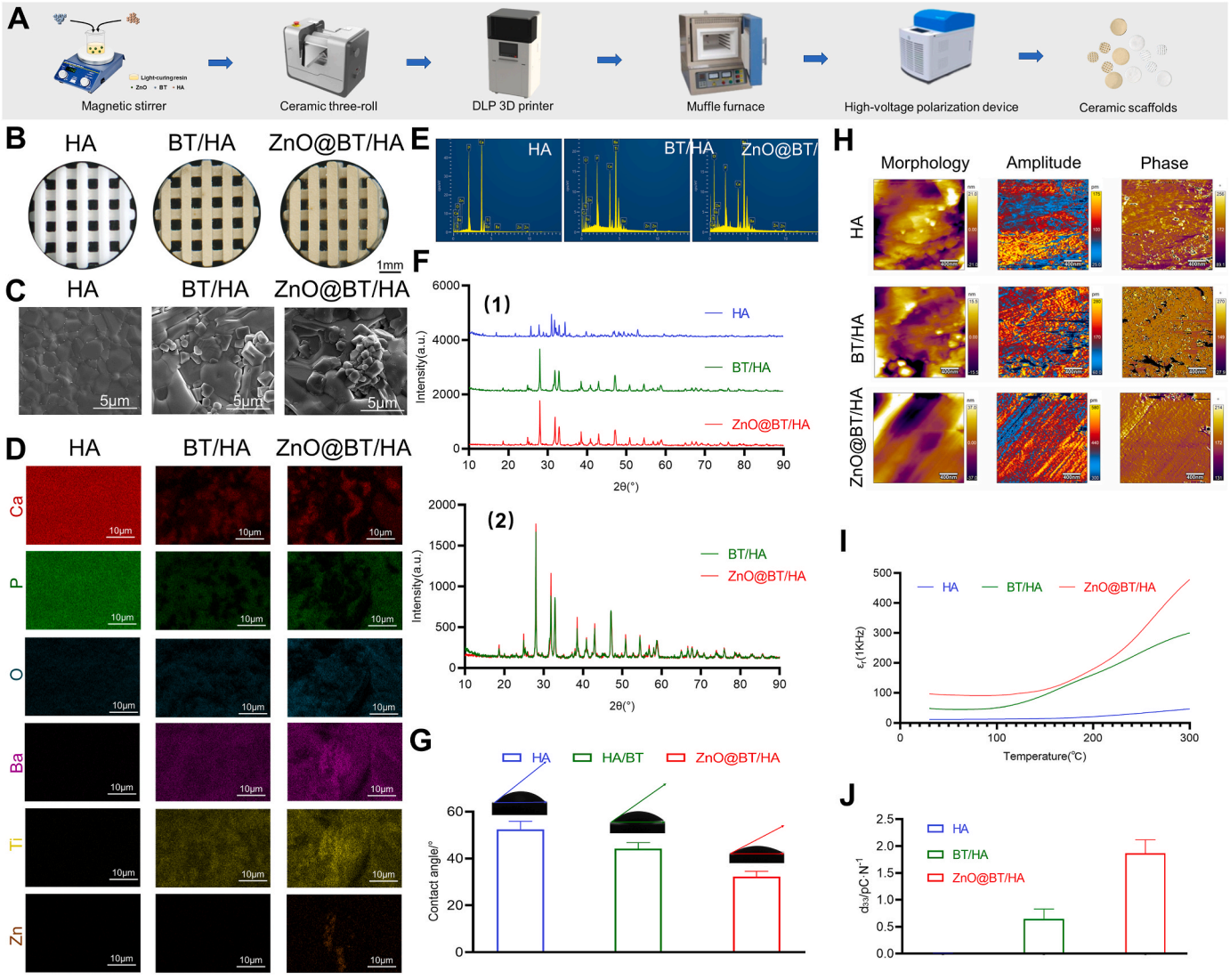

Fig. 1. Characterization of different groups of piezoelectric ceramic samples
A: The preparation processes of the 3D printed piezoelectric ceramic simples. B: Panoramic images of the 3D printed ceramic scaffolds. C: The SEM images of the 3D printed ceramic simples. D: The EDS mapping of the 3D printed ceramic simples. E: The EDX mapping of the 3D printed ceramic simples. F: The XRD pattern of the 3D printed ceramic simples. G: The water contact angle of the 3D printed piezoelectric ceramic simples at a RT. H: The morphology, amplitude and phase of the 3D printed piezoelectric ceramic simples. I: The relative dielectric (εr) of the 3D printed piezoelectric ceramic simples at a frequency of 1 KHz. J: The d_{33} of the 3D printed piezoelectric ceramic simples.

BT/HA, and ZnO@BT/HA ceramic samples were 52.34°, 44.17°, and 32.28°, respectively, and these results were significant ($p < 0.05$). The lower water contact angle indicates greater hydrophilicity. Consequently, ZnO@BT/HA ceramic samples, being more hydrophilic than the other two groups, are more conducive to cell adhesion [50].

In our previous investigation, by fine-tuning the HA to BT ratio, we observed that a BT content of 80 % in the system resulted in a piezoelectric constant d33 of 2.15 pC/N [51]. However, this configuration only allowed for 20 % HA. Aiming to enhance the HA content while maintaining piezoelectric performance, this study explores the improvement of piezoelectric properties in lead-free BT ceramics through ZnO-NPs doping. ZnO-NPs, known for their efficacy as a sintering aid, have been shown to enhance the sintering efficiency of ceramics [17]. Our comparative analysis reveals that incorporating 1 wt% ZnO-NPs into pure BT ceramics significantly enhances their electrical characteristics. Specifically, the εr value at the Curie temperature increased from 1879.8 to 3933.0, and the piezoelectric constant d33 rose from 35.68 pC/N to 83.83 pC/N [51]. This highlights the significant impact of 1 wt% ZnO-NPs on the electrical properties of BT ceramics, attributable to enhanced spontaneous polarizatio [47]. The electrical characteristics of the ceramic scaffolds, namely their relative dielectric constants (εr) and piezoelectric coefficient (d_{33}), for HA, BT/HA, and ZnO@BT/HA compositions (Fig. 1G and H). Fig. 1G shows the εr values at a frequency of 1 KHz. Notably, the εr of pure HA is significantly low at 37 °C, registering at 11.8. The incorporation of BT into the system markedly increases the εr to 46.9. Furthermore, the introduction of 1 wt % ZnO-NPs into the BT/HA composite more than doubles the εr to 95.0, emphasizing the considerable impact of trace ZnO-NPs in enhancing the εr of the BT-based system [47]. Fig. 1H examines the piezoelectric properties of these scaffolds. Measured with a quasi-static d_{33} tester, the d_{33} value of pure HA is negligible (0). The addition of BT results in a d_{33} value of 0.65 pC/N for the BT/HA composite. Remarkably, the inclusion of 1 wt% ZnO-NPs in the ZnO@BT/HA system elevates the d_{33} to 1.87 pC/N, aligning with the range of natural bone (0.7–2.3 pC/N) [48].

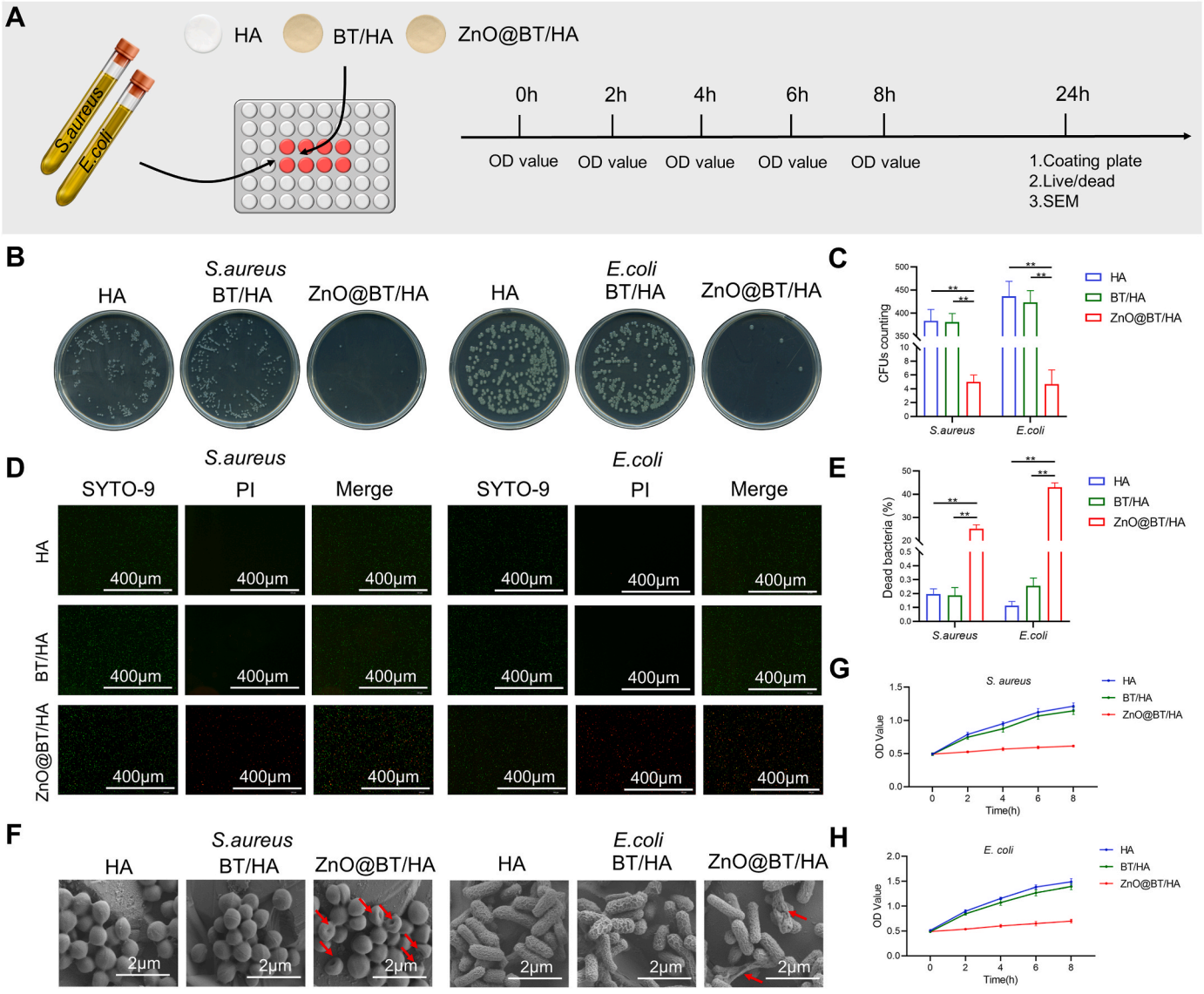

Fig. 2. In vitro antibacterial properties of different groups of piezoelectric ceramic samples
A: The process of antibacterial experiment of ceramic samples. B: The results of plate counting of the 3D printed ceramic simples. C: The quantitative results of CFU of the 3D printed ceramic simples. D: The live/dead bacterial staining of the 3D printed ceramic simples, green represents living bacteria and red represents dead bacteria. E: The quantitative proportion of dead bacteria of the 3D printed ceramic simples. F: The bacterial morphology scanning of the 3D printed piezoelectric ceramic simples. G: The plot growth curves of S. aureus after co-culture with 3D printed ceramic simples. H: The plot growth curves of E. coli after co-culture with 3D printed ceramic simples.

Different ceramics exhibit varied polarization response processes due to their microstructural differences [52]. The topography and piezoelectric response mode images of a 2 μm × 2 μm scanning area were tested, presenting representative topography, amplitude, and phase images in Fig. 1H. The morphology in Fig. 1H was omitted as it represented only the surface condition without additional electrical data. The amplitude and phase of the piezoelectric response signal relate to the magnitude of the piezoelectric coefficient and the direction of local polarization, respectively [53]. In the piezoelectric response amplitude images, yellow indicates greater piezoelectricity, and blue indicates weaker piezoelectricity. The irregular light-dark contrast region in the phase result diagram indicates anti-parallel polarization domains [54]. The amplitude results show that the ZnO@BT/HA ceramic scaffold has a higher amplitude than the other two groups, suggesting stronger piezoelectric properties. This finding underscores the potential of ZnO@BT/HA ceramic scaffolds for applications requiring piezoelectric properties similar to those of biological tissues.

2.3. In vitro antibacterial experiment

ZnO-NPs enhance the properties of BT piezoelectric ceramics, refining their electrical attributes during sintering and introducing essential antibacterial capabilities into bone tissue engineering scaffold systems [44]. To explore the antibacterial efficacy of these materials, prevalent pathogens such as the Gram-positive bacterium S. aureus and the Gram-negative bacterium E. coli were selected for this study.

The results from the plate counting method are depicted in Fig. 2B, and the quantitative CFU counts are presented in Fig. 2C. Notably, the ZnO@BT/HA composite doped with ZnO-NPs exhibited pronounced antibacterial activity against S. aureus, demonstrated by a significant reduction in CFU counts ($p < 0.01$), compared to the HA and BT/HA groups. Similarly, for E. coli, the ZnO@BT/HA group showed substantial antibacterial properties, evidenced by a comparable reduction in CFU counts ($p < 0.01$). The live/dead bacterial staining results shown in Fig. 2D, and the quantitative analysis of dead bacteria proportions in Fig. 2E, further confirm the antibacterial efficacy. For both S. aureus and E. coli, the ZnO@BT/HA group contained a higher proportion of dead bacteria and fewer live bacteria than the HA and BT/HA groups. Specifically, dead S. aureus constituted 25.2 % of the total area, while dead E. coli accounted for 43.1 %, both representing significant differences ($p < 0.01$). These results highlight the bactericidal nature of ZnO@BT/HA ceramic samples, capable of eliminating a substantial portion of adhered pathogens. SEM imaging analysis of bacterial morphology revealed contrasting patterns between the groups. Bacteria on HA and BT/HA samples maintained their normal size, shape, and membrane integrity (Fig. 2F). Conversely, bacteria cultured on ZnO@BT/HA samples exhibited abnormal morphologies and shrunken membranes, indicative of stress or damage. Growth curves, constructed from absorbance values measured at various time points post-co-culture wit HA, BT/HA, and ZnO@BT/HA, are presented in Fig. 2G and H. These curves demonstrate that ZnO@BT/HA significantly impeded the growth of both S. aureus and E. coli, compared to the HA and BT/HA groups ($p < 0.01$), underscoring the potent antibacterial properties of ZnO@BT/HA and its suitability for applications requiring antimicrobial capabilities.

ZnO is highly regarded within the pharmaceutical industry and has been approved by the Food and Drug Administration (FDA) [55]. ZnO-NPs epossess a broad antibacterial spectrum, effectively inhibiting bacterial growth through membrane disruption, zinc ion release, and generation of intracellular reactive oxygen species (ROS) [4,5,56,57]. Therefore, ZnO-NPs are considered an optimal choice for combating antibiotic-resistant bacteria [58]. Given these properties, ZnO-NPs were selected as an additive in this study to enhance the antimicrobial qualities of BT/HA piezoelectric ceramic systems. In vitro antibacterial assays have conclusively shown the strong inhibitory effect of ZnO-NPs against both S. aureus and E. coli. Although BT is known to have some antibacterial potential, its efficacy requires nanoscale particles and ultrasonic stimulation [59,60]. In this study, BT particles were sized between 0.6 and 1 μm, and no ultrasonic stimulation was used during antibacterial testing. Thus, the BT/HA ceramic sample displayed antibacterial efficacy similar to that of the HA sample, consistent with previous findings [27].

2.4. In vitro biosafety

The CCK-8 assay results, shown in Fig. 3B, reveal trends in cell viability across various groups on days 1, 3, and 5. Notably, the HA and BT/HA groups displayed similar cell viability, with a significant difference emerging only on day 5. The addition of 1 wt% ZnO-NPs significantly enhanced cell activity and proliferation in the ZnO@BT/HA group ($p < 0.05$). Moreover, the integration of polarization and LIPUS in the LP-ZnO@BT/HA group resulted in the highest cell viability, distinct from the other groups ($p < 0.05$), highlighting the synergistic effects of these factors. Live/dead cell staining images in Fig. 3C differentiate viable (green) and nonviable (red) cells. The quantitative analysis in Fig. 3D shows cell death rates. No significant difference was observed in the proportion of dead cells between the HA and BT/HA groups, while the ZnO@BT/HA group showed a reduction in dead cells, though not significant ($p > 0.05$). The LP-ZnO@BT/HA group had the lowest rate of dead cells among all groups, significantly so ($p < 0.05$), demonstrating the effectiveness of this treatment in preserving cell viability. Fluorescent staining was used to assess the cytoskeletal architecture and nuclear features of DPSCs, highlighting F-actin with rhodamine-phalloidin and nuclei with Hoechst, as displayed in Fig. 3E. The LP-ZnO@BT/HA group exhibited fuller cell morphology compared to the other groups, indicating enhanced cellular development. The cytoplasm-to-nucleus (C/N) ratio of DPSCs was analyzed in Fig. 3F. No significant difference in the C/N ratio was found between the HA and BT/HA groups. However, a significant increase in the C/N ratio was noted with the addition of 1 wt % ZnO-NPs ($p < 0.05$), indicating cellular growth and maturation. Remarkably, the LP-ZnO@BT/HA group, exposed to polarization and LIPUS, showed the highest C/N ratio among all groups ($p < 0.05$). This increase in C/N ratio correlates with the natural process of cell development, characterized by cytoplasmic expansion, thus serving as an indicator of increased cell maturity [61], highlighting the beneficial effects of the LP-ZnO@BT/HA treatment on DPSCs maturation.

Optimal concentrations of ZnO-NPs have been demonstrated to enhance cell proliferation [46]. Biocompatibility assessments showed that DPSCs cultured on ZnO@BT/HA ceramic samples, modified with ZnO-NPs, exhibited significantly enhanced proliferation capabilities compared to those on HA and BT/HA surfaces. Additionally, a notable reduction in the rate of cell death was observed in the ZnO@BT/HA group. Moreover, the C/N ratio in the ZnO@BT/HA group, augmented by ZnO-NPs, exceeded that of the initial groups, confirming that this ZnO-NP-modified ceramic system promotes cellular maturation without cytotoxicity.

DPSCs cultured on LP-ZnO@BT/HA surfaces demonstrated substantial improvements in cellular activity and proliferation capacity, surpassing the first three groups. This improvement was accompanied by a notable decrease in the rate of dead cells and a significant increase in the nuclear proportion, indicating peak cellular maturity. The significant changes in the biological behavior of DPSCs on LP-ZnO@BT/HA ceramic samples, compared to ZnO@BT/HA, are attributed to the synergistic effects of LIPUS and piezoelectric properties. LIPUS is believed to play a crucial role in modulating the biological responses of DPSCs, including proliferation and activity. Research by Gao and colleagues has shown that LIPUS (at intensities of 250/750 mW/cm^2, 1 MHz, administered for 5 or 10 min per day) stimulates DPSC proliferation, with 250 mW/cm2 producing the most pronounced effects [62]. Furthermore, the integration of LIPUS causes the polarized piezoceramic surface to generate electrical energy, immersing DPSCs in a microelectric environment that triggers alterations in their biological behavior [63,64]. This highlights the multifaceted benefits of the LP-ZnO@BT/HA system

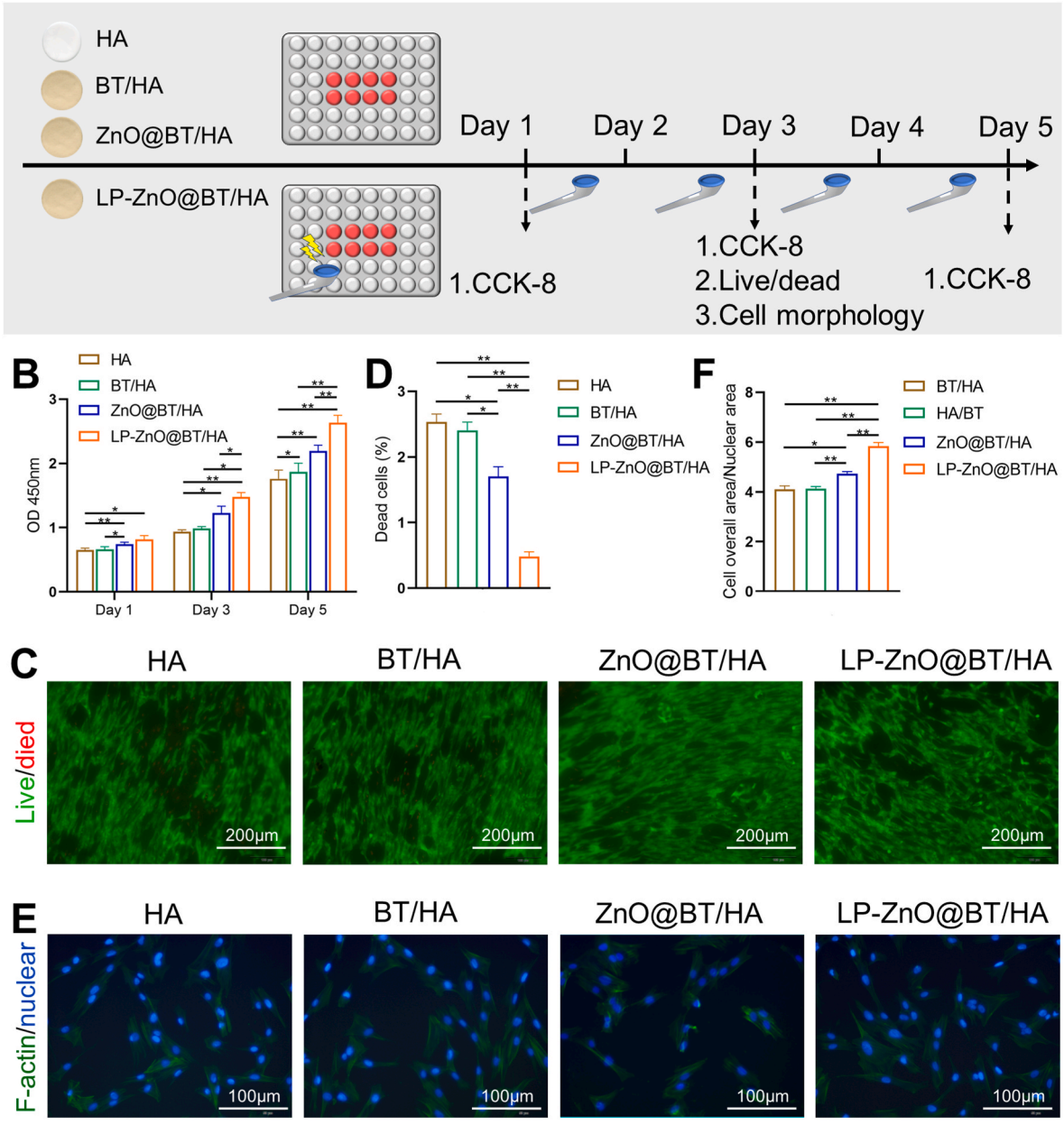

Fig. 3. In vitro biosafety of different groups of piezoelectric ceramic samples
A: The process of in vitro biosafety test of ceramic samples. B: The results of CCK-8 assay of the 3D printed ceramic simples. C: The live/dead cell staining of the 3D printed ceramic simples, green represents living cells and red represents dead cells. D: The quantitative proportion of dead cells of the 3D printed ceramic simples. E: F-actin and nucleus results of DPSCs after 3 days of co-culture with different groups of ceramic samples, green represents F-actin and blue represents dead nucleus. F: Quantitative results of C/N ratio.

in promoting optimal DPSC development and functionality.

2.5. *In vitro osteogenic properties*

Osteogenic induction medium was applied to DPSCs on various ceramic surfaces for 7 days, with ALP staining outcomes illustrated in Fig. 4B. Despite varying background hues among the groups, LP-ZnO@BT/HA surfaces showed pronounced purple agglomerations, indicating superior osteogenic properties. To reduce the effect of background color variations on our results, hexadecylpyridinium chloride monohydrate was used in an elution process, detailed in Fig. 4C. This approach enabled clearer visualization of the LP-ZnO@BT/HA group, enriched with ZnO-NPs and enhanced by LIPUS stimulation. The darker hue of eluents from this group highlighted its increased osteogenic capacity in vitro, outperforming the other groups. Quantitative analysis of eluent color, shown in Fig. 4D, supports these findings. While no significant differences were observed between the HA and BT/HA groups, the addition of ZnO in the ZnO@BT/HA group led to a notable increase in osteogenic activity. The LP-ZnO@BT/HA group, enhanced synergistically by LIPUS and polarization, displayed the highest OD value among all groups. Immunofluorescence (IF) staining results in Fig. 4E show OCN in red, OPN in green, and nuclei stained blue. Detailed microscopic imagery reveals that the LP-ZnO@BT/HA group exhibits the highest expression levels of both OCN and OPN proteins. Further quantitative analysis of fluorescence intensity, as shown in Fig. 4F, reveals consistent trends in protein expression. No significant differences were noted between the HA and BT/HA groups, but ZnO-NPs significantly elevated OCN and OPN protein expression in DPSCs. The LP-

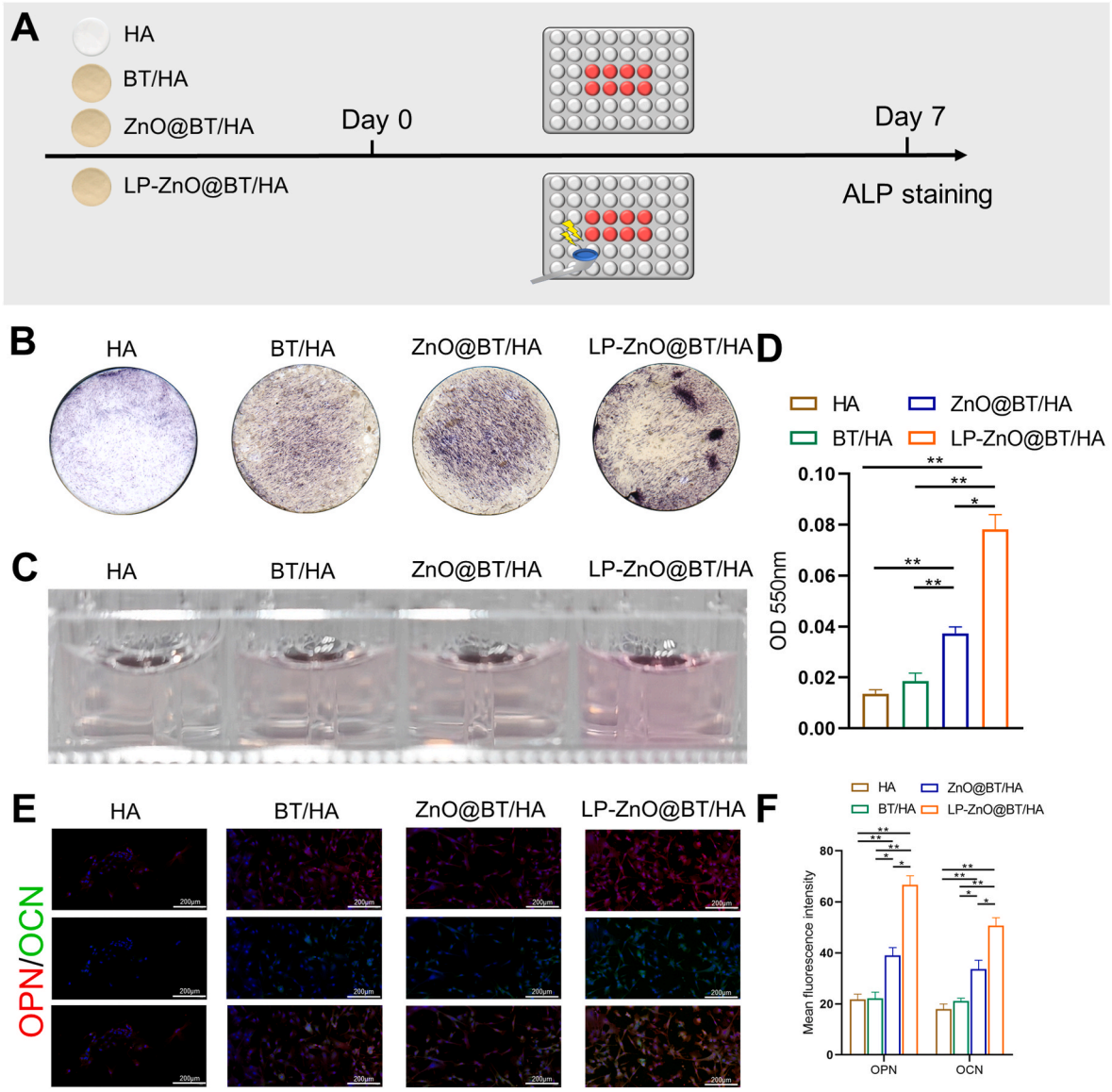

Fig. 4. In vitro osteogenic properties of different groups of piezoelectric ceramic samples
A: The process of in vitro osteogenic properties test of ceramic samples. B: ALP staining assays results of DPSCs after 7 days of co-culture with different groups of ceramic samples. C: Color comparison of eluents harvested from different groups of ceramic samples after ALP staining assays. D: The quantitative analysis of eluents harvested from different groups of ceramic samples after ALP staining assays. E: Immunofluorescence staining assays results of DPSCs after 7 days of co-culture with different groups of ceramic samples (red for OPN, green for OCN, blue for nucleus). F: The quantitative analysis results of immunofluorescence staining of different groups of ceramic samples.

ZnO@BT/HA group demonstrated the highest protein levels among the groups tested.

Numerous studies have shown that incorporating ZnO into bone tissue engineering scaffolds significantly enhances MSC osteogenic differentiation capabilities, marking a notable advancement in the field [65–67]. Additionally, many studies have recognized that LIPUS can stimulate MSC osteogenic differentiation through various biological pathways, highlighting its potential as a powerful therapeutic tool [68–70]. Since the discovery of bone tissue's piezoelectric properties, a range of materials with these unique characteristics have been utilized to promote osteogenic differentiation, offering innovative therapeutic options for bone defects [71–73]. This study highlights the remarkable enhancement of osteogenic properties in ceramic samples through the incorporation of ZnO-NPs. Furthermore, the combined effect of LIPUS and the piezoelectric properties significantly amplifies the osteogenic efficacy of the ceramic system, corroborating previous research findings.

2.6. *In vitro angiogenic properties*

Achieving efficient vascularization is crucial in bone tissue engineering to enhance the regenerative potential of scaffold materials [74]. This process ensures an ample nutrient supply and facilitates oxygen exchange and metabolic activities of osteoblasts, the primary bone-forming cells [75]. Consequently, this study examined DPSCs' migratory abilities and the expression patterns of vasogenesis-associated proteins across various ceramic sample groups. Fig. 5B illustrates the migratory behavior of DPSCs on different ceramic samples. Additionally, Fig. 5C presents a quantitative assessment of wound healing, offering a detailed understanding of the process. The results showed that DPSCs in both the HA and BT/HA groups exhibited comparable migratory capabilities. However, the inclusion of ZnO-NPs enhanced the migration potential of DPSCs. Significantly, the integration of LIPUS and piezoelectric effects into the experimental setup led to a marked improvement ($p < 0.05$) in the migratory abilities of DPSCs, highlighting

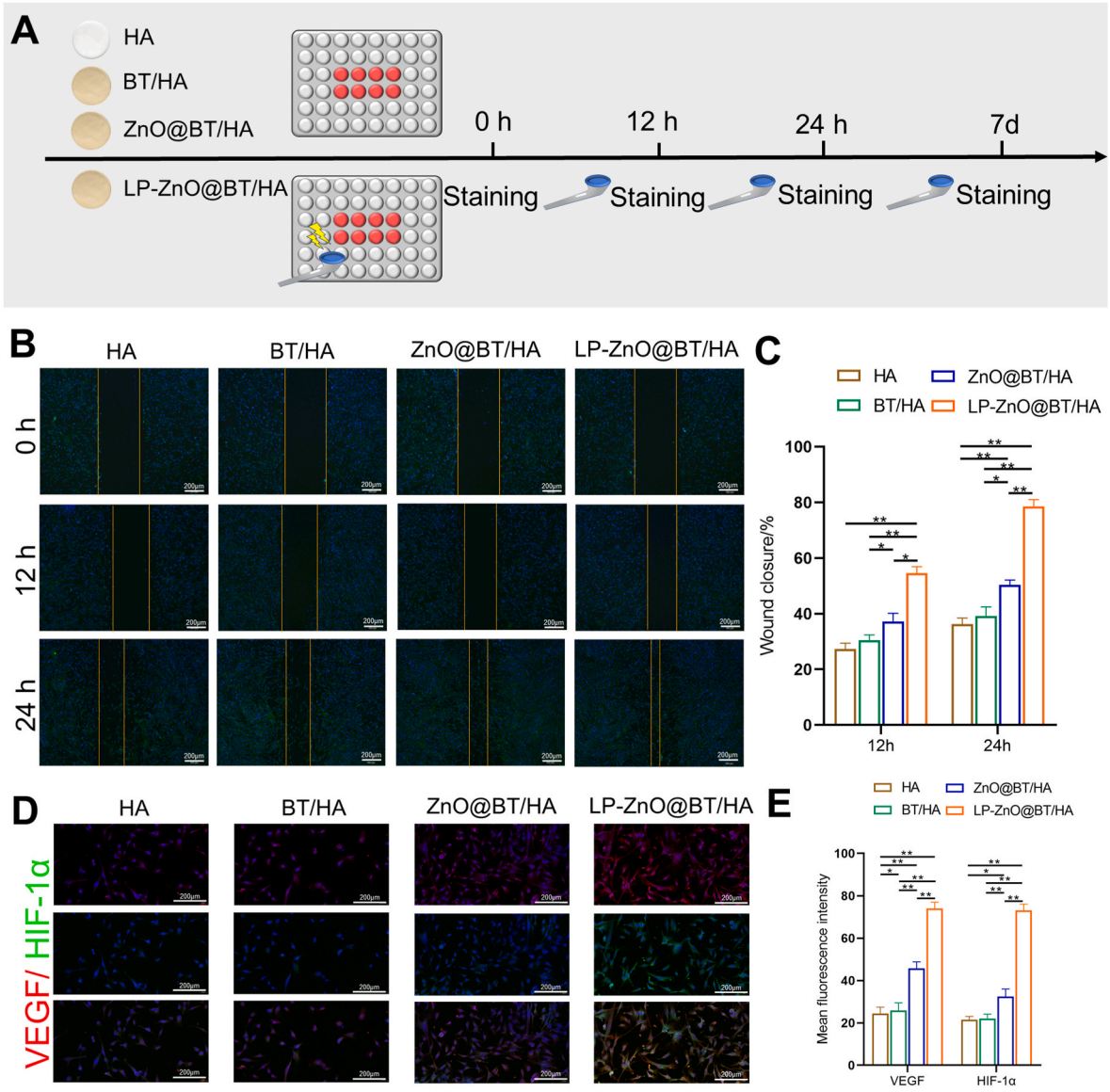

Fig. 5. In vitro angiogenic properties of different groups of piezoelectric ceramic samples
A: The process of in vitro angiogenic properties test of ceramic samples. B: The cell scratch assay results of DPSCs in different groups of ceramic samples. C: The quantitative analysis of wound healing rate results in different groups of ceramic samples at different time points. D: The quantitative analysis of eluents harvested from different groups of ceramic samples after ALP staining assays. D: Immunofluorescence staining assays results of DPSCs after 7 days of co-culture with different groups of ceramic samples (red for VEGF, green for HIF-1α, blue for nucleus). E: The quantitative analysis results of immunofluorescence staining of different groups of ceramic samples.

the synergistic benefits of these factors. IF staining results, shown in Fig. 5D, illustrate the distribution of VEGF (red), HIF-1α (green), and nuclei (blue). The LP-ZnO@BT/HA group displayed the most pronounced expression levels of the osteogenic markers VEGF and HIF-1α proteins. Quantitative analysis of fluorescence intensity, presented in Fig. 5E, revealed a consistent pattern of significant upregulation of VEGF and HIF-1α proteins in DPSCs following the incorporation of ZnO-NPs, emphasizing their critical role in promoting vascularization. The LP-ZnO@BT/HA group exhibited the highest concentrations of VEGF and HIF-1α proteins among the groups, underscoring its outstanding vascularization potential.

Studies have demonstrated that LIPUS can promote angiogenic differentiation of MSCs through various signaling pathways [76,77]. Additionally, the piezoelectric effect in tissue engineering scaffolds has been shown to enhance the angiogenic differentiation of MSCs [78,79]. This study highlights the profound impact of combining LIPUS and the piezoelectric effect on facilitating MSC migration and enhancing the expression of vasogenic proteins. This evidence further validates its ability to stimulate vasogenic differentiation of MSCs, emphasizing its potential in regenerative medicine.

2.7. Transcriptomics analysis

To explore the molecular mechanisms behind the osteogenic enhancement observed in LP-ZnO@BT/HA ceramic samples, a comprehensive transcriptomic analysis was conducted comparing the control group with the LP-ZnO@BT/HA treatment group (Fig. 6). Initial differential gene statistics identified changes in gene expression profiles between these groups, as illustrated in Fig. 6B. The differential gene volcano plot revealed a significant finding: 531 genes showed differential expression, with 256 up-regulated and 275 down-regulated due to LP-ZnO@BT/HA treatment. Notably, the EGR1 gene was the most prominently altered among the upregulated genes. To visually display these extensive transcriptional changes, a heat map including all 531

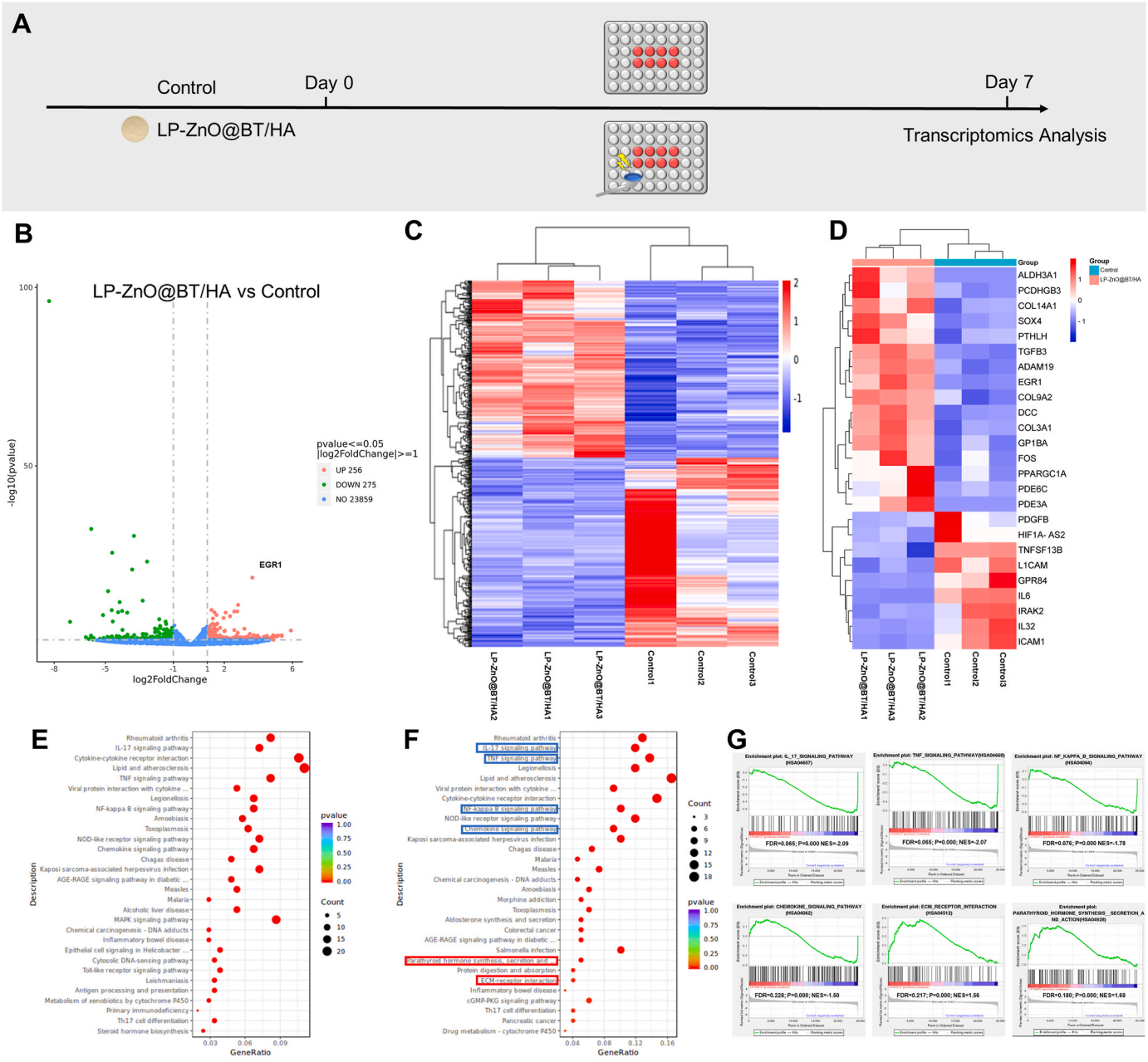

Fig. 6. The results of transcriptomics analysis of osteogenesis
A: The process of transcriptomics analysis of osteogenesis. B: Differential gene volcano plot of LP-ZnO@BT/HA group and control group. C: Differential gene heat map of LP-ZnO@BT/HA group and control group. D: Heat maps of some osteogenic differential genes in LP-ZnO@BT/HA group and control group. E: The KEGG enrichment of all differential gene. F: The KEGG enrichment of upregulated and downregulated genes (blue indicating downregulation, red indicating upregulation). G: Signaling pathways associated with osteogenesis analyzed in part by GSEA enrichment.

differential genes was created, shown in Fig. 6C. A subset of genes related to osteogenesis was specifically highlighted in Fig. 6D, emphasizing their roles in the noted osteogenic enhancement. Deeper insights were sought through Kyoto Encyclopedia of Genes and Genomes (KEGG) enrichment analysis, the results of which are depicted in Fig. 6E. This analysis segregated the upregulated and downregulated genes into distinct KEGG pathways, identifying specific signaling cascades, marked by blue and red boxes in Fig. 6F (blue for downregulation, red for upregulation), as crucial to the osteogenic differentiation of MSCs. Notably, it was hypothesized that the LP-ZnO@BT/HA ceramic scaffold promotes osteogenic differentiation in DPSCs via the "Parathyroid hormone synthesis, secretion, and action" signaling pathway. Furthermore, Gene Set Enrichment Analysis (GSEA) pathway analysis corroborated these findings, reinforcing the proposed molecular mechanisms at play.

Previous research has highlighted the significant role of EGR1 as a key transcription factor in growth and differentiation processes [80,81]. Research on dental stem cells from apical papilla and dental follicle indicated that EGR1 actively promotes osteogenic differentiation, potentially through the modulation of distal-less homeobox 3 and bone morphogenetic protein 2 expression [82]. Further studies confirmed EGR1's essential role in osteogenic differentiation of MSCs in response to mechanical stimuli [83]. Additionally, recent research demonstrated EGR1's role in enhancing chondrogenic differentiation of MSCs, facilitated by a complex silk-based hydrogel, showcasing its versatility in stem cell fate regulation [84]. In this study, whole-transcriptome sequencing was used to analyze gene expression differences between

the LP-ZnO@BT/HA group and the control group, revealing significant upregulation of the EGR1 gene in the LP-ZnO@BT/HA group. Both KEGG pathway analysis and GSEA highlighted the critical role of the "Parathyroid Hormone Synthesis, Secretion, and Action" pathway in promoting osteogenic differentiation of DPSCs within the LP-ZnO@BT/HA treatment framework. In conclusion, transcriptome profiling indicated that LIPUS and piezoelectric effects work together to enhance osteogenic differentiation of DPSCs by specifically upregulating the EGR1 gene within this signaling cascade, thus uncovering a novel mechanism for improved bone regeneration in ceramic materials.

2.8. In vivo osteogenic and angiogenic properties

Infected scaffolds were first utilized to assess in vivo antimicrobial performance. Supplementary Figs. 4B and 4C shows a significant reduction in bacterial colonies in the ZnO@BT/HA and LP-ZnO@BT/HA groups compared to the HA and BT/HA groups, demonstrating effective antibacterial activity of ZnO-doped piezoelectric ceramic scaffolds in vivo.

Following the encouraging in vitro results regarding osteogenic and angiogenic potential, a deeper investigation into the ability of various ceramic scaffolds to stimulate in vivo bone regeneration was conducted using a standardized rat skull defect model with a well-defined defect diameter ($\varphi = 5$ mm) [85]. Additionally, to explore the antibacterial efficacy of ZnO-NPs-doped scaffolds, an infected skull defect model was employed. Micro-CT analyses, detailed in Fig. 7B–F, provide intricate insights. To ensure unbiased imaging and quantitative assessment of nascent bone tissue, scaffolds and bone tissue were meticulously reconstructed in isolation. Examination of the two-dimensional images across groups (Fig. 7B) revealed that HA and BT/HA ceramic scaffolds exhibited suboptimal contact with adjacent bone tissue, appearing as low-density regions. Conversely, scaffolds doped with ZnO-NPs, specifically ZnO@BT/HA and LP-ZnO@BT/HA, showed seamless integration with surrounding bone tissue. Three-dimensional reconstructions of new bone tissue (Fig. 7B) indicated that while HA and BT/HA scaffolds displayed comparable osteogenic efficacy in vivo, the inclusion of ZnO-NPs significantly enhanced the osteogenic capability of the ZnO@BT/HA scaffold. Moreover, when combined with polarization and LIPUS stimulation, the LP-ZnO@BT/HA group was the most effective at inducing bone regeneration, outperforming other groups at both 4 and 8 weeks' assessment points. Quantitative analysis of 3D reconstructed structures, including BV/TV, Tb.Th, Tb.N, and Tb. Sp. Was conducted to evaluate new bone formation (Fig. 5C–F). At 4 and 8 weeks post-surgery, there were no significant differences in BV/TV, Tb.Th, Tb.N, and Tb. Sp between the HA and BT/HA groups, except that BT/HA showed higher Tb. Th at 8 weeks. Significant statistical differences were observed in BV/TV, Tb.Th, Tb.N, and Tb. Sp in the ZnO@BT/HA group compared to the first two groups. With LIPUS stimulation and the polarization process, BV/TV, Tb.Th, and Tb.N in the LP-ZnO@BT/HA group significantly increased, and Tb. Sp significantly decreased compared to the other groups.

H&E and Masson's trichrome staining are commonly used histological methods to evaluate potential inflammatory responses associated with scaffold implantation and to assess collagen synthesis and bone maturation [86]. The H&E staining results revealed no notable severe inflammation across all groups, confirming the exceptional biocompatibility of the implanted ceramic scaffolds (Fig. 7G). In vivo biosafety findings further support this observation (Supplementary Fig. 5). Masson's staining showed a lighter hue for the HA and BT/HA groups, while the ZnO@BT/HA and LP-ZnO@BT/HA groups exhibited deep dark-blue staining, indicative of robust collagen deposition. Additionally, the red staining in these groups highlighted the organized structure of the calcified extracellular matrix (Fig. 7H). By week 8, the new bone had nearly filled the defect and enveloped the LP-ZnO@BT/HA scaffold, with trabecular morphology resembling autologous bone. These results highlight a significant disparity in osteogenic potential, with ZnO-NPs-doped ZnO@BT/HA and LP-ZnO@BT/HA groups exhibiting far superior abilities compared to the HA and BT/HA groups. The ZnO@BT/HA group, enriched with ZnO-NPs, showed a heightened capacity for bone formation over the initial two groups. Combined with LIPUS stimulation and polarization effects, the LP-ZnO@BT/HA scaffolds emerged as the most potent osteogenic enhancers, outperforming all other groups.

Eight weeks post-implantation, the rat skulls were subjected to IF staining, revealing significant findings (Fig. 8). To assess osteogenesis and angiogenesis at the defect sites, antibodies against osteogenic markers Runx2, COL1, OCN, and OPN, as well as angiogenic markers TGF-β, ANG-1, VEGF, and HIF-1α were used. A meticulous quantitative analysis displayed a nuanced trend: although the BT/HA group showed slightly higher levels than the HA group, this difference was not significant. Notably, the incorporation of ZnO-NPs significantly enhanced both angiogenic and osteogenic potential. Furthermore, the integration of LIPUS and piezoelectric effects dramatically increased the scaffold's capacity to stimulate angiogenesis and promote bone regeneration, making it the most effective among the four experimental groups.

Previous studies have shown that incorporating ZnO-NPs onto biomaterial surfaces accelerates bone integration of implants and shortens the healing period [7]. Additionally, these studies have highlighted the ability of ZnO-NPs to stimulate bone differentiation in MSCs [3,46]. ZnO also possesses strong antibacterial properties that facilitate the regeneration of infected bone defects [3,87,88], prompting the development of an infected skull defect model in this study.

Our results indicate that ZnO-NPs-doped ZnO@BT/HA ceramic samples demonstrate enhanced osteogenic potential both in vitro and in vivo compared to their ZnO-NPs-free counterparts. Specifically, these samples promote osteogenic differentiation of DPSCs in vitro and effectively stimulate bone regeneration in vivo within infected skull defect models. Notably, the LP-ZnO@BT/HA ceramic sample outperformed the other three groups in terms of osteogenic efficacy, emphasizing the synergistic effect of LIPUS stimulation and polarization [89]. LIPUS is known to promote osteogenesis through various signaling pathways that augment the expression of osteogenic proteins [90]. Our observations align with previous findings showing LIPUS enhancing osteogenic differentiation in MSCs [91]. Besides its direct osteogenic impact, LIPUS acts as an exogenous inducer, converting mechanical energy from piezoelectric materials into electrical energy, thereby enhancing its osteogenic effect [50,89,92]. Thus, our study highlights the significant osteogenic effects of LP-ZnO@BT/HA ceramic samples, achieved through dual stimulation by LIPUS and the piezoelectric effect. This innovative approach offers considerable potential for advancing bone regeneration strategies in cases of infected bone defects.

3. Materials and methods

3.1. Preparation and characterization ceramic simples

3.1.1. Materials

Highly purified ZnO-NPs (99.8 % purity), with an initial particle size of D50 = 50 ± 10 nm, were obtained from Aladdin in Shanghai, China. BT (99.9 % purity), with a particle size range of D50 = 0.6–1 μm, was sourced from Mackin in Dalian, China. HA (97 % purity), with a particle size of D50 < 100 nm, was also procured from Aladdin to ensure consistent quality. For 3D printing, a specialized light-curing resin was formulated, primarily consisting of polyethylene glycol (600) dimethacrylate (PEG600DMA, 80 %), γ-(methylallyl) propyl trimethoxysilane (KH-570, 15 %), 2,4,6-trimethylbenzoyl-diphenyl oxide phosphine (TPO-L, 2 %), and Sudan red, following a previously established recipe [45]. This resin blend is optimized for performance in the 3D printing process [51].

3.1.2. Preparation of ceramic simples (Fig. 1A)

The fabrication of 3D printed piezoelectric ceramic specimens was

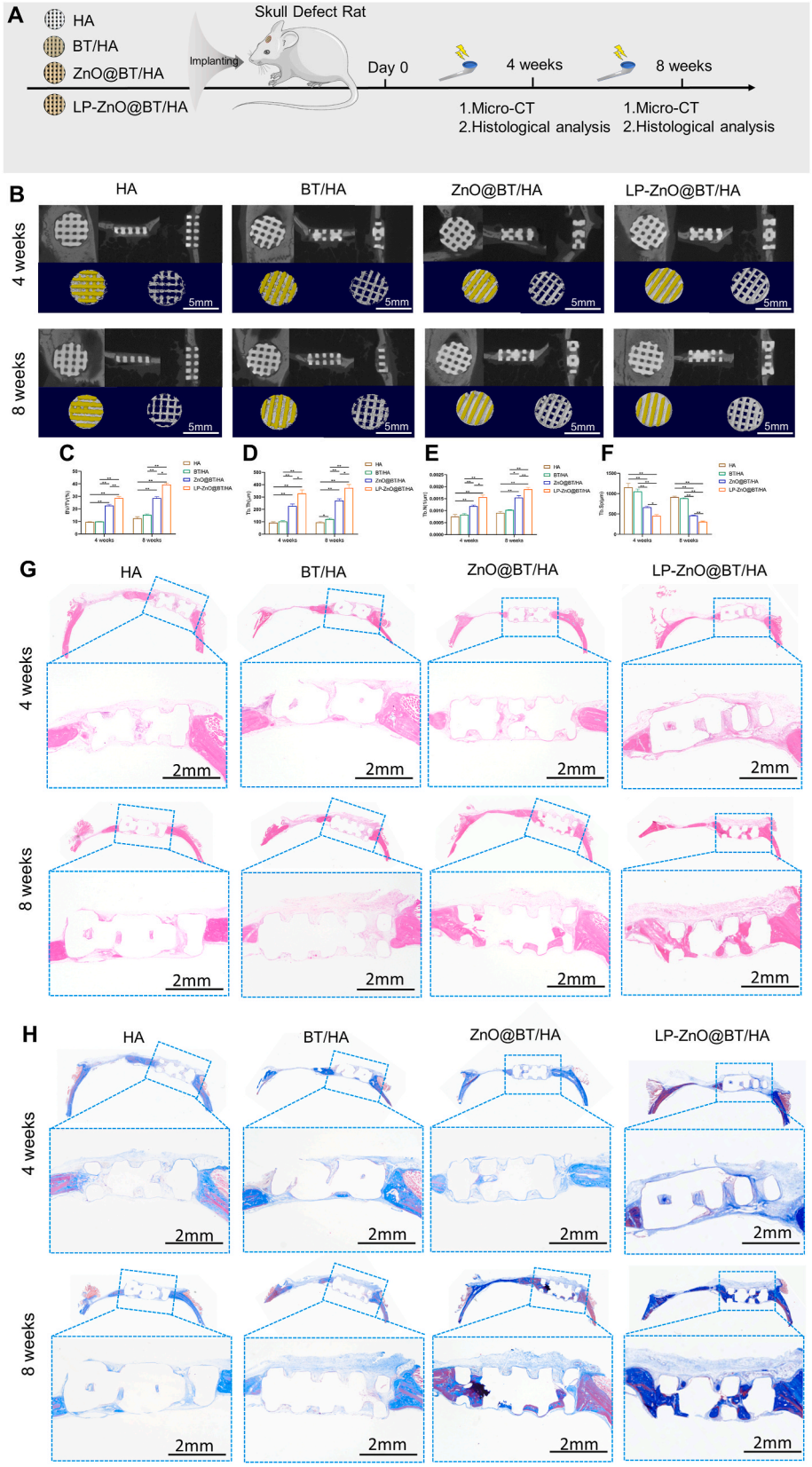

Fig. 7. In vivo osteogenic properties of different groups of piezoelectric ceramic samples
A: The process of in vivo osteogenic properties test of ceramic samples. B: Two-dimensional images of bone defects combined with ceramic scaffolds and 3D reconstruction of the new bone tissue with/without ceramic scaffolds. C: The quantitative results of BV/TV of the 3D printed ceramic simples. D: The quantitative results of Tb.Th of the 3D printed ceramic simples. E: The quantitative results of Tb.N of the 3D printed ceramic simples. F: The quantitative results of Tb. Sp of the 3D printed ceramic simples. G: The H&E staining results of the 3D printed ceramic simples. H: The Masson's trichrome staining results of the 3D printed ceramic simples.

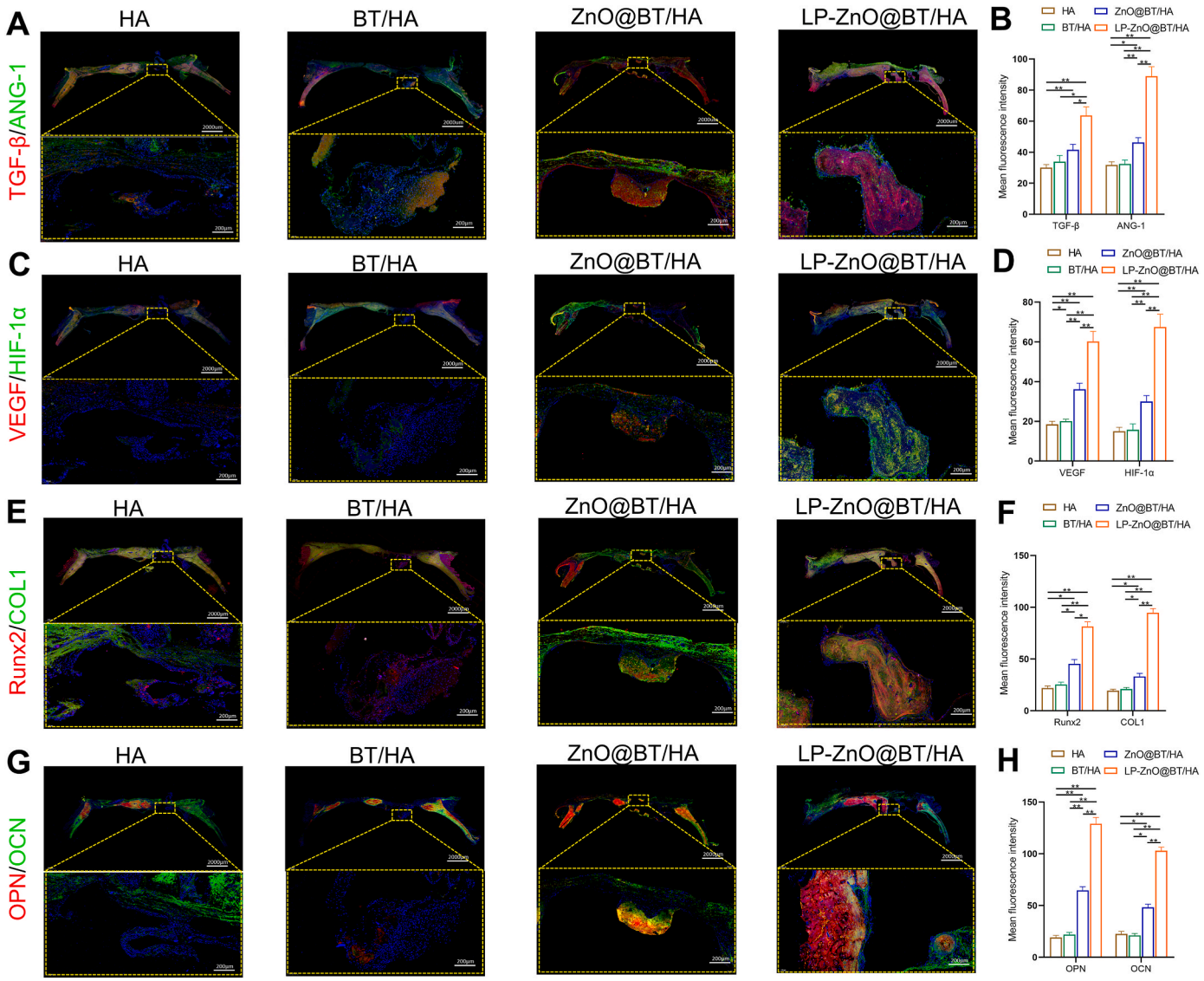

Fig. 8. Results of immunofluorescence staining of osteogenesis and angiogenesis in vivo
A: TGF-β and ANG-1 protein expression in different ceramic scaffold groups (red for TGF-β, green for ANG-1, blue for nucleus). B: The quantitative analysis of TGF-β and ANG-1 protein expression in different ceramic scaffold groups. C: VEGF and HIF-1α protein expression in different ceramic scaffold groups (red for VEGF, green for HIF-1α, blue for nucleus). D: The quantitative analysis of VEGF and HIF-1α protein expression in different ceramic scaffold groups. E: Runx2 and COL1 protein expression in different ceramic scaffold groups (red for Runx2, green for COL1, blue for nucleus). F: The quantitative analysis of Runx2 and COL1 protein expression in different ceramic scaffold groups. G: OPN and OCN protein expression in different ceramic scaffold groups (red for OPN, green for OCN, blue for nucleus). H: The quantitative analysis of OPN and OCN protein expression in different ceramic scaffold groups.

conducted following methods from previous studies [51]. Initially, ZnO-NPs were homogeneously dispersed within a light-curing resin matrix using a magnetic stirrer. Subsequently, varying concentrations of BT and HA were meticulously blended with the ZnO-NPs-laden resin using a precision ceramic three-roll mill. The ceramic scaffolds and discs were then constructed using a DLP 3D printer, adhering to optimized printing parameters: light intensity of 2.5 mW/cm2, exposure time of 10 s, and a layer thickness of 20 μm. After printing, the specimens underwent a thorough degreasing process and were sintered in a muffle furnace at 1250 °C for 2 h to ensure high-quality consolidation. In the next step, the ceramic samples were subjected to high-voltage polarization in a specialized device, applying a field strength of 30 kV/cm for 20 min at room temperature to enhance their piezoelectric properties. Prior to further experimentation, any silver coating applied during the fabrication process was meticulously removed. Finally, the prepared piezoelectric ceramic scaffolds and discs were ready for subsequent experimental evaluations and applications.

3.1.3. Scanning electron microscope (SEM), X-ray diffraction (XRD), and water contact angle

To examine the detailed morphology and microstructure of the ceramic samples, a SEM (Oxford ULTIM Max65 model) was utilized. The samples were carefully sputter-coated with gold to improve image clarity and enable high-resolution imaging. SEM acquisitions were performed at an optimized accelerating voltage of 10 kV. Additionally, energy-dispersive spectroscopy (EDS) in mapping mode was employed to visualize the spatial distribution of key elements within the samples, providing crucial insights into their in-situ elemental composition. For phase composition analysis, comprehensive XRD assessments were carried out using a Bruker D8 Advance instrument over a 2θ range of 10°–90°, with a scanning rate of 10°/min and a step size of 0.02°. The surface water contact angle of the ceramic samples was measured using a contact angle meter (OCA-20, Germany) through the sessile-drop method at room temperature. A 5 μL droplet of deionized water was placed on the sample surface, and the droplet's shape was captured.

Three different points on each sample were tested, and the average value was calculated.

3.1.4. Dielectric properties and piezoelectric properties

The dielectric characteristics of the ceramic samples were analyzed utilizing a high-precision dielectric temperature spectrometer (DMS-500, China), covering a frequency range from 1 kHz to 1 MHz and temperature range from 30 °C to 300 °C. The piezoelectric properties were evaluated using a quasi-static d_{33} tester (ZJ-3AN, China), examining the samples under pressurization ranging from −10 to 10 V at a frequency of 75 Hz. Additionally, piezoelectric force microscopy (PFM, Asylum Research + Cypher ES, USA) was used to analyze morphology, amplitude, and phase displacement of the piezoelectric response.

3.2. In vitro antibacterial experiment (Fig. 2A)

3.2.1. Bacteria culture

In this study, the antibacterial efficacy of the samples was evaluated against two bacterial strains: the Gram-positive Staphylococcus aureus (S. aureus, ATCC 29213) and the Gram-negative Escherichia coli (E. coli ATCC 25922). These bacteria served as model organisms to assess the antimicrobial properties of three distinct ceramic categories: HA (pure HA), BT/HA (a blend of HA and BT in a 70BT/30HA ratio), and ZnO@BT/HA (addition of 1 wt% ZnO-NPs to the previous BT/HA ratio). The study systematically investigated the impact of various ceramic compositions on antibacterial performance against these strains.

3.2.2. Antibacterial activity

The antibacterial efficacy was rigorously assessed using the plate count method. A 500-μL bacterial suspension, adjusted to an optical density (OD) of 0.5 at 600 nm, was thoroughly mixed with each sample and incubated at 37 °C for 24 h. Post-incubation, a 20-μL aliquot from the diluted co-cultured bacterial suspension was carefully inoculated onto Luria-Bertani (LB) agar plates to promote the growth of bacterial colonies. The antibacterial prowess of the samples was quantitatively evaluated by meticulously counting the colony-forming units (CFUs) on the agar surfaces.

3.2.3. Live/dead bacterial staining

A 500-μL bacterial suspension, standardized to an OD600 of 0.5, was intimately mixed with various samples and incubated at 37 °C for 24 h. Bacterial cells adhering to the samples were differentially stained using equal volumes of SYTO 9 and propidium iodide (PI), producing distinct green and red fluorescent signatures for 20 min. High-resolution images were captured using an advanced fluorescence microscope (OLYMPUS IX71, Japan) for analysis. The proportion of non-viable (dead) bacteria was quantified using Image-Pro Plus software, enabling precise assessment of the samples' antibacterial effectiveness.

3.2.4. Bacterial morphology scanning

Following a 24-h incubation at 37 °C, 500 μL of bacterial suspension, standardized to an OD600 of 0.5, were exposed to various samples, then fixed with paraformaldehyde for 60 min. After triple rinsing with phosphate-buffered saline (PBS), the samples were dehydrated using a graded ethanol series (25 %, 50 %, 75 %, and 100 %), facilitating preservation of bacterial morphology. The dried samples were coated with a thin gold layer via spray-gold process, enhancing their SEM imaging conductivity. Using an advanced SEM instrument (JEOL JSM-3400IV), the morphology of the adhered bacteria was visualized in detail, providing insights into their interactions with the sample surfaces.

3.2.5. Absorbance test

5 mL of bacterial suspension, adjusted to an OD600 of 0.5, were exposed to diverse samples and incubated at 37 °C for 8 h. The absorbance at 600 nm was meticulously measured at 2-h intervals during this period, allowing for the monitoring of bacterial growth dynamics.

3.3. In vitro biosafety (Fig. 3A)

3.3.1. Cell culture

Dental pulp stem cells (DPSCs) were extracted and cultured according to established methodologies, using Alpha Modified Eagle Medium (α-MEM) (Gibco, China), supplemented with 10 % fetal bovine serum (FBS) (Biological Industries, Israel) and 1 % penicillin–streptomycin, at 37 °C in a 5 % CO_2 in a humidified incubator. Ceramic samples were grouped as follows: HA (pure HA), BT/HA (70BT/30HA combination), ZnO@BT/HA (addition of 1 wt% ZnO-NPs to BT/HA), and LP-ZnO@BT/HA (polarized ZnO@BT/HA stimulated by LIPUS). The LIPUS stimulation protocol is outlined in a prior publication [43]. Briefly, the LIPUS exposure was conducted in vitro using a Sonicator 740 device (Mettler Electronics, USA), which delivered a 1 MHz sine wave, a 50 % duty cycle, and an intensity of 30 mW/cm^2. A custom-designed water-filled apparatus served as the platform for LIPUS application, with a 48-well plate positioned on the water's surface. This setup facilitated the non-invasive stimulation of DPSCs attached to the sample surfaces in the wells, using water as the coupling medium. The LIPUS treatment was administered daily for 10 min at 37 °C.

3.3.2. Cell viability and proliferation assay

Following the arrangement of various ceramic samples in a 48-well plate, dental pulp stem cells (DPSCs) were seeded onto each and cultured over periods of 1, 3, and 5 days. Cell proliferation and viability were assessed using the sensitive Cell Counting Kit-8 (CCK-8) from Dojindo (Japan).

3.3.3. Live/dead cell staining

After placing various ceramic samples in a 48-well plate, DPSCs were seeded onto these substrates and cultured for 3 days. The cells were then stained using a Live/Dead Cell Staining Kit (LMAI, China), which uses Calcein AM and PI to emit green and red fluorescence, respectively, distinguishing live from dead cells. The fluorescence-based differentiation was examined under an Olympus IX71 high-resolution fluorescence microscope (Japan), and images were captured for detailed analysis. Image-Pro Plus software was used to quantify the precise proportion of dead cells, providing a quantitative assessment of cellular health and vitality in response to the ceramic environments.

3.3.4. Cell morphology

Various ceramic samples were placed in a 48-well plate and DPSCs were seeded onto these surfaces, where they were cultured for 3 days. The cells were fixed with 4 % paraformaldehyde for 15 min at 4 °C to preserve structural integrity, followed by permeabilization with 0.1 % Triton-X 100 for 10 min at room temperature to facilitate staining. The cytoskeleton was stained with rhodamine-phalloidin (Solarbio, China) for 20 min at room temperature, producing a vibrant red fluorescence. Nuclei were counterstained with Hoechst 33342 (Solarbio, China) for 1 min at room temperature, resulting in a distinct blue fluorescence for clear delineation of cellular structures. These fluorescently labeled samples were examined under the advanced optics of an Olympus IX71 fluorescence microscope (Japan), and images were captured for subsequent analysis. Image-Pro Plus software quantified cellular morphology, specifically measuring the ratio of overall cellular area to nuclear area (CN rate), across different groups, providing a quantitative assessment of cellular growth on the ceramic substrates.

3.4. In vitro osteogenic properties (Fig. 5A)

3.4.1. Alkaline phosphatase (ALP) staining

Osteogenic differentiation was induced in DPSCs cultured on various samples using a medium containing 10 mM β-glycerophosphate, 10 nM dexamethasone, and 50 mg/mL ascorbic acid for 7 days. ALP activity

was performed using the BCIP/NBT Alkaline Phosphatase Color Development Kit (Beyotime, China). To reduce color interference from HA and BT materials, cells were de-stained with 10 % hexadecylpyridinium chloride monohydrate (Aladdin, China) at room temperature, and the eluates were analyzed in a 96-well plate at 550 nm using an enzyme-labeling instrument (Biotech, USA).

3.4.2. IF staining and analysis

The assessment of protein expression levels of osteocalcin (OCN) and osteopontin (OPN) in co-cultured DPSCs was conducted using IF Staining techniques. To induce osteogenic differentiation, DPSCs were co-cultured with ceramic samples in 48-well plates immersed in osteogenic induction medium for 7 days. Afterward, the DPSCs were fixed with 4 % paraformaldehyde for 15 min and washed thoroughly with PBS, repeating the wash step three times. IF staining involved antibodies from Servicebio, China, including Rabbit Monoclonal Antibody against OCN, Rabbit Monoclonal Antibody against OPN, HRP-labeled Goat Anti-rabbit IgG, and Alexa Fluor 488-labeled Goat Anti-rabbit IgG, following the manufacturer's protocols. Additionally, nuclei were stained with DAPI (Servicebio, China) to enhance the visualization of cellular structures. IF images were captured and analyzed using Image-Pro Plus software, which enabled the quantification of average fluorescence intensity of the proteins, providing a detailed assessment of the expression levels of OCN and OPN in the co-cultured DPSCs.

3.5. In vitro angiogenic properties (Fig. 5A)

3.5.1. Cell scratch assay

Dental pulp stem cells (DPSCs) were seeded on ceramic samples in 48-well plates and incubated for 12 h at 37 °C in a 5 % CO2 atmosphere to facilitate cell adhesion and monolayer formation. A wound model was then created on the ceramic surface using a 200 μl pipette tip. Cytoskeleton and nucleus staining were performed at 0h, 12h, and 24h to monitor in vitro wound closure. The scratch width was measured to calculate the wound healing extent, with the closure rate determined by: (original width - measured width)/original width * 100 %.

3.5.2. IF staining and analysis

Protein expression levels of vascular endothelial growth factor (VEGF) and hypoxia-inducible factor 1α (HIF-1α) in co-cultured DPSCs were analyzed using IF staining. To induce osteogenic differentiation, DPSCs were cultured with ceramic samples in osteogenic induction medium for 7 days. The cells were then fixed with 4 % paraformaldehyde for 15 min and washed three times with PBS. IF staining utilized Servicebio antibodies, including Rabbit Monoclonal Antibodies against VEGF and HIF-1α, HRP-labeled Goat Anti-rabbit IgG, and Alexa Fluor 488-labeled Goat Anti-rabbit IgG, following manufacturer's instructions. Nuclei were stained with DAPI (Servicebio, China), enhancing cellular structure visualization. The images were captured and analyzed with Image-Pro Plus software to quantify the fluorescence intensity, thus assessing VEGF and HIF-1α expression levels in DPSCs.

3.6. Transcriptomics analysis of osteogenesis (Fig. 6A)

To elucidate the molecular mechanisms behind the osteogenic differentiation promoted by the LP-ZnO@BT/HA group, gene expression profiling was conducted. DPSCs were co-cultured with ceramic samples in osteogenic induction medium for 7 days. Transcriptome analysis identified differentially expressed genes, highlighting those up-regulated or down-regulated during osteogenic differentiation on LP-ZnO@BT/HA ceramic surfaces. Pathway analyses, including KEGG and GSEA, were performed to identify relevant pathways.

3.7. In vivo osteogenic properties (Fig. 7A)

3.7.1. Infected skull defect model and scaffold implantation

All animal experiments received approval from the Research Ethics Committee of the College of Basic Medical Sciences, Jilin University (Ethics number: 2022450). Eight-week-old male Sprague-Dawley (SD) rats, sourced from the Laboratory Animal Centre at Jilin University, were used to create calvaria critical-size defects. Twenty-four rats were divided into four groups (9 rats per group): Group I: HA alone, Group II: BT/HA mixture (70BT/30HA), Group III: ZnO@BT/HA (with 1 wt% ZnO-NPs), and Group IV: LP-ZnO@BT/HA (LIPUS-stimulated ZnO@BT/HA). Before surgery, the scaffolds (D: 5 mm, H: 1.5 mm) were contaminated with 10 μl S. aureus (OD600 = 0.5). Rats were anesthetized through intraperitoneal injection of sodium pentobarbital (10 mg/100 g body weight). Following anaesthesia, a critical-size defect of 5 mm diameter was created in the skull using a micro drill at low rotation speed with constant irrigation. Post-surgery, the LIPUS exposure device was immediately applied to the LP-ZnO@BT/HA group using the parameters previously described in the cell studies. Specifically, the ultrasound transducer was positioned on the skin of the head, secured by a thin layer of coupling agent, and maintained for 10 min daily over 1, 4, or 8 weeks. At 4 and 8 weeks post-implantation, the rats were euthanized using an overdose of CO2 to obtain the skull specimens containing the scaffold.

3.7.2. In vivo antibacterial activity (Supplementary Figure 4A)

After a week of implantation, the infected scaffolds were extracted, and bacteria were isolated using ultrasound. Twenty microliters of the bacterial suspension were plated on agar and incubated overnight before being counted and photographed.

3.7.3. Micro-computed tomography (Micro-CT) scanning and evaluation

Specimens, fixed in 4 % paraformaldehyde, underwent scanning with a Micro-CT scanner (PerkinElmer Quantum GX2, USA) at 90 kV source voltage, 88 μA beam current, and 25 μm resolution. Three-dimensional reconstruction was achieved using CTvol software (Bruker Micro-CT). The area of the scaffold (D: 5 mm, H: 1.5 mm) was identified as the region of interest (ROI). CTan software (Bruker Micro-CT) was used to calculate the percentage of bone volume to total volume (BV/TV), Trabecular Thickness (Tb.Th), Trabecular Number (Tb.N), and Trabecular Space (Tb.Sp).

3.7.4. Histological and histomorphometric analysis

Skull tissues were fixed and decalcified for 28 days, followed by dehydration and embedding in paraffin. Bone slices were then stained with Hematoxylin-Eosin (H&E) and Masson's trichrome stains.

3.7.5. IF analysis

Skull tissues from eight-week specimens were fixed and subjected to 28 days of decalcification, then dehydrated and embedded in paraffin. IF staining was conducted on these sections. Osteogenesis-related antibodies (Anti-runt-related transcription factor-2 (Runx2), collagen type 1 (COL1), OCN, and OPN) and angiogenesis-related antibodies (Anti-transforming growth factor β (TGF-β), angiopoietin 1 (ANG-1), VEGF, and HIF-1α) were applied to assess osteogenesis and angiogenesis at defect sites in rats. Images were captured and analyzed using Image-Pro Plus software to quantify the average fluorescence intensity and protein expression levels.

3.7.6. In vivo biosafety

At four weeks, rat hearts, livers, spleens, lungs, and kidneys were harvested, dehydrated, and embedded for histological examination to assess in vivo toxicity via H&E staining.

3.8. Statistics

All data were presented as mean ± standard deviation (SD). Statistical analyses were performed using SPSS 19.0 and GraphPad Prism 8 (GraphPad Software, San Diego, CA, USA), with significance thresholds set at $p = 0.05$. Discrepancies between groups were indicated with asterisks: *$p < 0.05$, **$p < 0.01$.

4. Conclusion

This study utilized DLP 3D printing technology to fabricate a ZnO-modified BT/HA piezoelectric ceramic scaffold for repairing infected bone defects. Firstly, the piezoelectric properties of the ZnO-modified BT were enhanced, facilitating an increased HA content in the scaffold. Secondly, the scaffold demonstrated significant antibacterial efficacy in vitro. Additionally, with the incorporation of LIPUS and piezoelectric effects, the scaffold exhibited superior osteogenic capabilities. Thus, the development of multifunctional bone tissue engineering ceramic scaffolds holds promising potential for the repair of complex tissue defects [93].

Ethics approval and consent to participate

All animal experiments received approval from the Research Ethics Committee of the College of Basic Medical Sciences, Jilin University (Ethics number: 2022450).

CRediT authorship contribution statement

Kai Chen: Writing – original draft, Methodology, Investigation, Funding acquisition, Data curation, Conceptualization. **Fang Wang:** Writing – review & editing, Resources, Funding acquisition, Data curation. **Xiumei Sun:** Methodology, Investigation. **Wenwei Ge:** Visualization, Software, Resources, Methodology. **Mingjun Zhang:** Software, Resources, Methodology. **Lin Wang:** Software, Methodology. **Haoyu Zheng:** Resources, Methodology. **Shikang Zheng:** Validation, Software, Methodology. **Haoyu Tang:** Resources, Methodology. **Zhengjie Zhou:** Software, Methodology. **Guomin Wu:** Writing – review & editing, Project administration, Funding acquisition, Conceptualization.

Declaration of competing interest

The authors declare that they have no known competing financial interests or personal relationships that could have appeared to influence the work reported in this paper.

Acknowledgements

This study was supported by grants from National Key R&D Project of China, Ministry of Science and Technology of the People's Republic of China (grant numbers: 2023YFC2509205), Jilin Provincial Science and Technology Development Project (grant numbers: 20230204088YY), Jlin Provincial Science and Technology Development Project (grant numbers: YDZJ202401300ZYTS), Fund Project of Science and Technology Project of Jilin Provincial Department of Finance (grant numbers: JCSZ2023481-15), Jilin Provincial Key Laboratory of Precision Infectious Diseases (grant numbers: 20200601011JC), Jilin Province Development and Reform Commission (grant numbers: 2022C036), and Graduate Innovation Fund of Jilin University (grant numbers: 2024CX127).

Appendix A. Supplementary data

Supplementary data to this article can be found online at https://doi.org/10.1016/j.bioactmat.2024.11.015.

References

[1] C.T. Johnson, J.A. Wroe, R. Agarwal, K.E. Martin, R.E. Guldberg, R.M. Donlan, L. F. Westblade, A.J. García, Hydrogel delivery of lysostaphin eliminates orthopedic implant infection by Staphylococcus aureus and supports fracture healing, Proc. Natl. Acad. Sci. U.S.A. 115 (22) (2018) E4960–e4969.
[2] P.P. Kalelkar, M. Riddick, A.J. García, Biomaterial-based delivery of antimicrobial therapies for the treatment of bacterial infections, Nat. Rev. Mater. 7 (1) (2022) 39–54.
[3] Y. Zhang, Z. Li, B. Guo, Q. Wang, L. Chen, L. Zhu, T. Zhang, R. Wang, W. Li, D. Luo, et al., A zinc oxide nanowire-modified mineralized collagen scaffold promotes infectious bone regeneration, Small (2023) e2309230.
[4] Y. Li, Y. Yang, Y. Qing, R. Li, X. Tang, D. Guo, Y. Qin, Enhancing ZnO-NP antibacterial and osteogenesis properties in orthopedic applications: a review, Int. J. Nanomed. 15 (2020) 6247–6262.
[5] S. Jha, R. Rani, S. Singh, Biogenic zinc oxide nanoparticles and their biomedical applications: a review, J. Inorg. Organomet. Polym. Mater. (2023) 1–16.
[6] S. Raha, M. Ahmaruzzaman, ZnO nanostructured materials and their potential applications: progress, challenges and perspectives, Nanoscale Adv. 4 (8) (2022) 1868–1925.
[7] Z. Wang, X. Wang, Y. Wang, Y. Zhu, X. Liu, Q. Zhou, NanoZnO-modified titanium implants for enhanced anti-bacterial activity, osteogenesis and corrosion resistance, J. Nanobiotechnol. 19 (1) (2021) 353.
[8] D.P. Kiouri, E. Tsoupra, M. Peana, S.P. Perlepes, M.E. Stefanidou, C.T. Chasapis, Multifunctional role of zinc in human health: an update, EXCLI journal 22 (2023) 809–827.
[9] Z. Neščáková, K. Zheng, L. Liverani, Q. Nawaz, D. Galusková, H. Kaňková, M. Michálek, D. Galusek, A.R. Boccaccini, Multifunctional zinc ion doped sol - gel derived mesoporous bioactive glass nanoparticles for biomedical applications, Bioact. Mater. 4 (2019) 312–321.
[10] M. Laurenti, V. Cauda, ZnO nanostructures for tissue engineering applications, Nanomaterials 7 (11) (2017).
[11] N. Bhadwal, R. Ben Mrad, K. Behdinan, Review of zinc oxide piezoelectric nanogenerators: piezoelectric properties, composite structures and power output, Sensors 23 (8) (2023).
[12] A. Shayan, M. Abdellahi, F. Shahmohammadian, S. Jabbarzare, A. Khandan, H. Ghayour, Mechanochemically aided sintering process for the synthesis of barium ferrite: effect of aluminum substitution on microstructure, magnetic properties and microwave absorption (vol 708, pg 538, 2017), J. Alloys Compd. 713 (2017), 18-18.
[13] U. Naresh, R.J. Kumar, N.V.S. Gupta, D. Kothandan, Ferroelectric properties of CuFe2O4, BaFe2O4, Ba0.2La0.8Fe2O4 nanoparticles, Elect. Sci. Eng. 1 (1) (2019) 6.
[14] R.K. Pandey, J. Dutta, S. Brahma, B. Rao, C.A.P. Liu, Review on ZnO-based piezotronics and piezoelectric nanogenerators: aspects of piezopotential and screening effect, Journal of Physics-Materials 4 (4) (2021).
[15] M. Promsawat, Z.-G. Ye, A. Watcharapasorn, Enhancement of piezoelectric properties of $Pb(Mg_{1/3}Nb_{2/3})$ $0.65Ti_{0.35}O_3$ ceramics by ZnO modification, Mater. Lett. 205 (2017) 126–129.
[16] X. Pang, J. Qiu, K. Zhu, J. Du, Effect of ZnO on the microstructure and electrical properties of $(K_{0.5}Na_{0.5})NbO_3$ lead-free piezoelectric ceramics, J. Mater. Sci. Mater. Electron. 23 (5) (2012) 1083–1086.
[17] S.-H. Lee, S.-G. Lee, H.-J. Kim, Y.-H. Lee, Effect of sintering temperature on piezoelectric and dielectric properties of $0.98(Na_{0.5}K_{0.5})NbO_3$-$0.02Li(Sb_{0.17}Ta_{0.83})O_3$+0.01wt%ZnO ceramics, J. Electroceram. 28 (2–3) (2012) 101–104.
[18] S.-H. Shin, J. Yoo, Effect of ZnO addition on dielectric and piezoelectric properties of $(Ba_{0.85}Ca_{0.15})(Ti_{0.915}Zr_{0.085})O_3$ ceramics, Ferroelectrics Lett. 42 (1–3) (2015) 43–50.
[19] D. Khare, B. Basu, A.K. Dubey, Electrical stimulation and piezoelectric biomaterials for bone tissue engineering applications, Biomaterials 258 (2020) 120280.
[20] E. Fukada, I. Yasuda, On the piezoelectric effect of bone 12 (10) (2007) 1158–1162.
[21] G.W. Hastings, Medicine FMJJoMSMi: the electromechanical properties of fluid-filled bone: a new dimension 2 (2) (1991) 118–124.
[22] R.V. Chernozem, M.A. Surmeneva, S.N. Shkarina, K. Loza, M. Epple, M. Ulbricht, A. Cecilia, B. Krause, T. Baumbach, A.A. Abalymov, et al., Piezoelectric 3-D fibrous poly(3-hydroxybutyrate)-based scaffolds ultrasound-mineralized with calcium carbonate for bone tissue engineering: inorganic phase formation, osteoblast cell adhesion, and proliferation, ACS Appl. Mater. Interfaces 11 (21) (2019) 19522–19533.
[23] S. Luo, C. Zhang, W. Xiong, Y. Song, Q. Wang, H. Zhang, S. Guo, S. Yang, H. Liu, Advances in electroactive biomaterials: through the lens of electrical stimulation promoting bone regeneration strategy, J Orthop Translat 47 (2024) 191–206.
[24] J. Li, Y. Xie, G. Liu, A. Bahatibieke, J. Zhao, J. Kang, J. Sha, F. Zhao, Y. Zheng, Bioelectret materials and their bioelectric effects for tissue repair: a review, ACS Appl. Mater. Interfaces 16 (30) (2024) 38852–38879.
[25] P. Wu, L. Shen, H.F. Liu, X.H. Zou, J. Zhao, Y. Huang, Y.F. Zhu, Z.Y. Li, C. Xu, L. H. Luo, et al., The marriage of immunomodulatory, angiogenic, and osteogenic capabilities in a piezoelectric hydrogel tissue engineering scaffold for military medicine, Military Medical Research 10 (1) (2023) 35.
[26] S. Joo, Y. Gwon, S. Kim, S. Park, J. Kim, S. Hong, Piezoelectrically and topographically engineered scaffolds for accelerating bone regeneration, ACS Appl. Mater. Interfaces 16 (2) (2024) 1999–2011.
[27] C. Lei, J. Lei, X. Zhang, H. Wang, Y. He, W. Zhang, B. Tong, C. Yang, X. Feng, Heterostructured piezocatalytic nanoparticles with enhanced ultrasound response for efficient repair of infectious bone defects, Acta Biomater. 172 (2023) 343–354.

[28] K.N.D.K. Muhsen, R.A.M. Osman, M.S. Idris, The effects of Ca, Zr and Sn substitutions into a ternary system of $BaTiO_3$-$BaSnO_3$-$BaZrO_3$towards its dielectric and piezoelectric properties: a review, J. Mater. Sci. Mater. Electron. 32 (10) (2021) 12771–12783.
[29] M. Adamczyk-Habrajska, B. Wodecka-Dus, T. Goryczka, D. Szalbot, M. Bara, L. Cieply, Dielectric and electric properties of $Ba_{0.996}La_{0.004}Ti_{0.999}O_3$ ceramics doped with europium and hafnium ions, Materials 15 (2) (2022).
[30] B. Deng, J. Jiang, H. Li, C. Zhao, C. Lin, X. Wu, M. Gao, T. Lin, Enhanced piezoelectric property in Mn-doped $K_{0.5}Na_{0.5}NbO_3$ ceramics via cold sintering process and $KMnO_4$ solution, J. Am. Ceram. Soc. 105 (9) (2022) 5774–5782.
[31] Q. Hou, B. Yang, C. Ma, Z. Zhou, R. Liang, H. Li, X. Dong, Tailoring structure and piezoelectric properties of $CaBi_2Nb_2O_9$ ceramics by W^{6+}-Doping, Ceram. Int. 48 (12) (2022) 16677–16684.
[32] Z. Peng, L. Chen, Y. Xiang, F. Cao, Microstructure and electrical properties of lanthanides-doped $CaBi_2Nb_2O_9$ ceramics, Mater. Res. Bull. 148 (2022).
[33] M. Du, Y. Li, Q. Zhang, J. Zhang, S. Ouyang, Z. Chen, The impact of low intensity ultrasound on cells: underlying mechanisms and current status. Progress in Biophysics and Molecular Biology, 2022.
[34] J.D. Heckman, J.P. Ryaby, J. McCabe, J.J. Frey, R.F. Kilcoyne, Acceleration of tibial fracture-healing by non-invasive, low-intensity pulsed ultrasound, J Bone Joint Surg Am 76 (1) (1994) 26–34.
[35] P.A. Nolte, A. van der Krans, P. Patka, I.M. Janssen, J.P. Ryaby, G.H. Albers, Low-intensity pulsed ultrasound in the treatment of nonunions, J. Trauma 51 (4) (2001) 693–702. ; discussion 702-693.
[36] X. Guo, M. Lv, J. Lin, J. Guo, J. Lin, S. Li, Y. Sun, X. Zhang, Latest progress of LIPUS in fracture healing: a mini-review, J. Ultrasound Med. : official journal of the American Institute of Ultrasound in Medicine (2024).
[37] S. Samaan, M.G. Sedhom, M.O. Grace, A randomized comparative study between high-intensity laser vs low-intensity pulsed ultrasound both combined with exercises for the treatment of knee osteoarthritis, Int J Rheum Dis 25 (8) (2022) 877–886.
[38] H. Raza, P. Major, D. Dederich, T. El-Bialy, Effect of low-intensity pulsed ultrasound on orthodontically induced root resorption caused by torque: a prospective, double-blind, controlled clinical trial, Angle Orthod. 86 (4) (2016) 550–557.
[39] X. Yang, Y. Wu, J. Li, W. Yin, Y. An, Y. Wang, M. Wang, Q. Wu, Z. Qu, G. Ning, et al., A pilot study of parameter-optimized low-intensity pulsed ultrasound stimulation for the bone marrow mesenchymal stem cells viability improvement, Comput. Math. Methods Med. 2019 (2019) 8386024.
[40] L. Ling, J. Hou, Y. Wang, H. Shu, Y. Huang, Effects of low-intensity pulsed ultrasound on the migration and homing of human amnion-derived mesenchymal stem cells to ovaries in rats with premature ovarian insufficiency, Cell Transplant. 31 (2022) 9636897221129171.
[41] Y. Wu, Q. Gao, S. Zhu, Q. Wu, R. Zhu, H. Zhong, C. Xing, H. Qu, D. Wang, B. Li, et al., Low-intensity pulsed ultrasound regulates proliferation and differentiation of neural stem cells through notch signaling pathway, Biochem. Biophys. Res. Commun. 526 (3) (2020) 793–798.
[42] Q. Liao, B.J. Li, Y. Li, Y. Xiao, H. Zeng, J.M. Liu, L.X. Yuan, G. Liu, Low-intensity pulsed ultrasound promotes osteoarthritic cartilage regeneration by BMSC-derived exosomes via modulating the NF-κB signaling pathway, Int. Immunopharm. 97 (2021) 107824.
[43] K. Chen, Y. Wang, C. Wu, Y. Du, H. Tang, S. Zheng, Z. Zhou, H. Zheng, G. Wu, Ln vitro assessment of immunomodulatory and osteogenic properties in 3D-printed hydroxyapatite/barium titanate piezoelectric ceramic scaffolds, Ceram. Int. 50 (6) (2024) 8751–8759.
[44] Z. Wen, X. Shi, X. Li, W. Liu, Y. Liu, R. Zhang, Y. Yu, J. Su, Mesoporous TiO2 coatings regulate ZnO nanoparticle loading and Zn2+Release on titanium dental implants for sustained osteogenic and antibacterial activity, ACS Appl. Mater. Interfaces 15 (12) (2023) 15235–15249.
[45] L. Taccola, V. Raffa, C. Riggio, O. Vittorio, M.C. Iorio, R. Vanacore, A. Pietrabissa, A. Cuschieri, Zinc oxide nanoparticles as selective killers of proliferating cells, Int. J. Nanomed. 6 (2011) 1129–1140.
[46] X. Wang, F. Shi, D. Zhao, Y. Yan, Effect of ZnO-doped magnesium phosphate cements on osteogenic differentiation of mBMSCs in vitro, J. Appl. Biomater. Funct. Mater. 20 (2022) 22808000221136369.
[47] A. Li, Y. Wang, Non-uniform micro-nanoarchitectonics of ZnO structure for the regulation of electrical properties of barium titanate lead-free piezoceramics, Appl. Phys. Mater. Sci. Process 128 (11) (2022).
[48] Y.F. Tang, C. Wu, Z.X. Wu, L. Hu, W. Zhang, K. Zhao, Fabrication and in vitro biological properties of piezoelectric bioceramics for bone regeneration, Sci. Rep. 7 (2017).
[49] E. Ul Haq, M.R.A. Karim, K.I. Khan, W. Akram, S.S. Hassan, F. Kashif, Study of structural and electrical properties of Zn-doped barium titanate ceramics synthesized by conventional solid-state method, J. Optoelectron. Adv. Mater. 24 (1–2) (2022) 69–73.
[50] B. Fan, Z. Guo, X. Li, S. Li, P. Gao, X. Xiao, J. Wu, C. Shen, Y. Jiao, W. Hou, Electroactive barium titanate coated titanium scaffold improves osteogenesis and osseointegration with low-intensity pulsed ultrasound for large segmental bone defects, Bioact. Mater. 5 (4) (2020) 1087–1101.
[51] K. Chen, Y. Wang, C. Wu, Y. Du, H. Tang, S. Zheng, Z. Zhou, H. Zheng, G. Wu, Ln vitro assessment of immunomodulatory and osteogenic properties in 3D-printed hydroxyapatite/barium titanate piezoelectric ceramic scaffolds, Ceram. Int. (2023).
[52] C. Wu, X. Qiu, W. Ge, L. Chen, C. Liu, H. Zhao, Z. Liu, L. Li, J.G. Fisher, A co-doping strategy to achieve high energy storage performance in $BiFeO_3$-based ceramics, Ceram. Int. 49 (17) (2023) 29218–29228.
[53] N. Jaitanong, H.R. Zeng, G.R. Li, Q.R. Yin, W.C. Vittayakorn, R. Yimnirun, A. Chaipanich, Interfacial morphology and domain configurations in 0-3 PZT-Portland cement composites, Appl. Surf. Sci. 256 (10) (2010) 3245–3248.
[54] S.M. Gheno, R.H.G.A. Kiminami, M.M. Morelli, J.V. Bellini, P.I. Paulin Filho, An AFM/EFM study of the grain boundary in ZnO-based varistor materials, J. Am. Ceram. Soc. 91 (11) (2008) 3593–3598.
[55] M. Kiarashi, P. Mahamed, N. Ghotbi, A. Tadayonfard, K. Nasiri, P. Kazemi, A. Badkoobeh, S. Yasamineh, A. Joudaki, Spotlight on therapeutic efficiency of green synthesis metals and their oxide nanoparticles in periodontitis, J. Nanobiotechnol. 22 (1) (2024) 21.
[56] Y. Li, J. Li, M. Li, J. Sun, X. Shang, Y. Ma, Biological mechanism of ZnO nanomaterials, J. Appl. Toxicol. : J. Anal. Toxicol. 44 (1) (2024) 107–117.
[57] S.M. George, C. Nayak, I. Singh, K. Balani, Multifunctional hydroxyapatite composites for orthopedic applications: a review, ACS Biomater. Sci. Eng. 8 (8) (2022) 3162–3186.
[58] H. Al-Momani, D. Al Balawi, S. Hamed, B.A. Albiss, M. Almasri, H. AlGhawrie, L. Ibrahim, H. Al Balawi, Haj Mahmoud S. Al, J. Pearson, et al., The impact of biosynthesized ZnO nanoparticles from Olea europaea (Common Olive) on Pseudomonas aeruginosa growth and biofilm formation, Sci. Rep. 13 (1) (2023) 5096.
[59] D. Liu, L. Li, B.L. Shi, B. Shi, M.D. Li, Y. Qiu, D. Zhao, Q.D. Shen, Z.Z. Zhu, Ultrasound-triggered piezocatalytic composite hydrogels for promoting bacterial-infected wound healing, Bioact. Mater. 24 (2023) 96–111.
[60] A. Houshyar, M. Ahmadian, Y. Azizian-Kalandaragh, N. Amirpour, H. Salehi, Fabrication and properties evaluation of chitosan/BaTiO(3) composite membranes for the periodontitis treatment, Sci. Rep. 14 (1) (2024) 1022.
[61] X. Wei, W. Zhou, Z. Tang, H. Wu, Y. Liu, H. Dong, N. Wang, H. Huang, S. Bao, L. Shi, et al., Magnesium surface-activated 3D printed porous PEEK scaffolds for in vivo osseointegration by promoting angiogenesis and osteogenesis, Bioact. Mater. 20 (2023) 16–28.
[62] Q. Gao, A.D. Walmsley, P.R. Cooper, B.A. Scheven, Ultrasound stimulation of different dental stem cell populations: role of mitogen-activated protein kinase signaling, J. Endod. 42 (3) (2016) 425–431.
[63] C. Shuai, G. Liu, Y. Yang, W. Yang, C. He, G. Wang, Z. Liu, F. Qi, S. Peng, Functionalized BaTiO(3) enhances piezoelectric effect towards cell response of bone scaffold, Colloids Surf. B Biointerfaces 185 (2020) 110587.
[64] K.K. Poon, M.C. Wurm, D.M. Evans, M.A. Einarsrud, R. Lutz, J. Glaum, Biocompatibility of (Ba,Ca)(Zr,Ti)O(3) piezoelectric ceramics for bone replacement materials, J. Biomed. Mater. Res. B Appl. Biomater. 108 (4) (2020) 1295–1303.
[65] S.V. Harb, E. Kolanthai, L.A. Pinto, C.A.G. Beatrice, E.O.T. Bezerra, E.H. Backes, L. C. Costa, S. Seal, L.A. Pessan, Additive manufacturing of bioactive and biodegradable poly (lactic acid)-tricalcium phosphate scaffolds modified with zinc oxide for guided bone tissue repair, Biomed. Mater. (2024).
[66] Y. Liu, L. Yu, J. Chen, S. Li, Z. Wei, W. Guo, Exploring the osteogenic potential of zinc-doped magnesium phosphate cement (zmpc): a novel material for orthopedic bone defect repair, Biomedicines 12 (2) (2024).
[67] Y. Zhang, Z. Li, B. Guo, Q. Wang, L. Chen, L. Zhu, T. Zhang, R. Wang, W. Li, D. Luo, et al., A zinc oxide nanowire-modified mineralized collagen scaffold promotes infectious bone regeneration, Small 20 (19) (2024) e2309230.
[68] T. Wu, F. Zheng, H.Y. Tang, H.Z. Li, X.Y. Cui, S. Ding, D. Liu, C.Y. Li, J.H. Jiang, R. L. Yang, Low-intensity pulsed ultrasound reduces alveolar bone resorption during orthodontic treatment via Lamin A/C-Yes-associated protein axis in stem cells, World J. Stem Cell. 16 (3) (2024) 267–286.
[69] S. Yan, D. Wang, L. Zhang, T. Gan, H. Yao, H. Zhu, Y. He, K. Yang, LIPUS-S/B@NPs regulates the release of SDF-1 and BMP-2 to promote stem cell recruitment-osteogenesis for periodontal bone regeneration, Front. Bioeng. Biotechnol. 11 (2023) 1226426.
[70] X. Li, Y. Zhong, W. Zhou, Y. Song, W. Li, Q. Jin, T. Gao, L. Zhang, M. Xie, Low-intensity pulsed ultrasound (LIPUS) enhances the anti-inflammatory effects of bone marrow mesenchymal stem cells (BMSCs)-derived extracellular vesicles, Cell. Mol. Biol. Lett. 28 (1) (2023) 9.
[71] Y. Chen, Y. Chen, Z. Xie, Y. Yang, S. Chen, T. Han, M. Li, Z. Guo, N. Sun, C. Wang, A biomimetic nanogenerator to enhance bone regeneration by restoring electric microenvironments, ACS Biomater. Sci. Eng. 10 (1) (2024) 525–536.
[72] H. Liu, Y. Shi, Y. Zhu, P. Wu, Z. Deng, Q. Dong, M. Wu, L. Cai, Bioinspired piezoelectric periosteum to augment bone regeneration via synergistic immunomodulation and osteogenesis, ACS Appl. Mater. Interfaces 15 (9) (2023) 12273–12293.
[73] S. Zhou, C. Xiao, L. Fan, J. Yang, R. Ge, M. Cai, K. Yuan, C. Li, R.W. Crawford, Y. Xiao, et al., Injectable ultrasound-powered bone-adhesive nanocomposite hydrogel for electrically accelerated irregular bone defect healing, J. Nanobiotechnol. 22 (1) (2024) 54.
[74] Z. Wang, Q. Dai, H. Luo, X. Han, Q. Feng, X. Cao, Nano-vibration exciter: hypoxia-inducible factor 1 signaling pathway-mediated extracellular vesicles as bioactive glass substitutes for bone regeneration, Bioact. Mater. 40 (2024) 460–473.
[75] M. Wu, H. Liu, Y. Zhu, P. Wu, Y. Chen, Z. Deng, X. Zhu, L. Cai, Bioinspired soft-hard combined system with mild photothermal therapeutic activity promotes diabetic bone defect healing via synergetic effects of immune activation and angiogenesis, Theranostics 14 (10) (2024) 4014–4057.
[76] F. Zhong, S. Cao, L. Yang, J. Liu, B. Gui, H. Wang, N. Jiang, Q. Zhou, Q. Deng, Low-intensity pulsed ultrasound accelerates diabetic wound healing by ADSC-derived exosomes via promoting the uptake of exosomes and enhancing angiogenesis, Int. J. Mol. Med. 53 (3) (2024).
[77] S. Liu, C. Jiang, J. Hu, H. Chen, B. Han, S. Xia, Low-intensity pulsed ultrasound enhanced adipose-derived stem cell-mediated angiogenesis in the treatment of

diabetic erectile dysfunction through the piezo-ERK-VEGF Axis, Stem Cell. Int. 2022 (2022) 6202842.
[78] W. Liu, X. Li, Y. Jiao, C. Wu, S. Guo, X. Xiao, X. Wei, J. Wu, P. Gao, N. Wang, et al., Biological effects of a three-dimensionally printed Ti6Al4V scaffold coated with piezoelectric BaTiO(3) nanoparticles on bone formation, ACS Appl. Mater. Interfaces 12 (46) (2020) 51885–51903.
[79] D. D'Alessandro, C. Ricci, M. Milazzo, G. Strangis, F. Forli, G. Buda, M. Petrini, S. Berrettini, M.J. Uddin, S. Danti, et al., Piezoelectric signals in vascularized bone regeneration, Biomolecules 11 (11) (2021).
[80] K. Tamama, D.J. Barbeau, Early growth response genes signaling supports strong paracrine capability of mesenchymal stem cells, Stem Cell. Int. 2012 (2012) 428403.
[81] E. Havis, D. Duprez, EGR1 transcription factor is a multifaceted regulator of matrix production in tendons and other connective tissues, Int. J. Mol. Sci. 21 (5) (2020).
[82] T. Press, S. Viale-Bouroncle, O. Felthaus, M. Gosau, C. Morsczeck, EGR1 supports the osteogenic differentiation of dental stem cells, Int. Endod. J. 48 (2) (2015) 185–192.
[83] W. Wang, N. Li, M. Wang, Y. Zhao, H. Wu, J. Shi, M. Musa, X. Chen, Analysis of ceRNA networks during mechanical tension-induced osteogenic differentiation of periodontal ligament stem cells, Eur. J. Oral Sci. 130 (5) (2022) e12891.
[84] Z. Cao, H. Wang, J. Chen, Y. Zhang, Q. Mo, P. Zhang, M. Wang, H. Liu, X. Bao, Y. Sun, et al., Silk-based hydrogel incorporated with metal-organic framework nanozymes for enhanced osteochondral regeneration, Bioact. Mater. 20 (2023) 221–242.
[85] P.S. Gomes, M.H. Fernandes, Rodent models in bone-related research: the relevance of calvarial defects in the assessment of bone regeneration strategies, Lab. Anim 45 (1) (2011) 14–24.
[86] L. Wang, Y. Pang, Y. Tang, X. Wang, D. Zhang, X. Zhang, Y. Yu, X. Yang, Q. Cai, A biomimetic piezoelectric scaffold with sustained Mg(2+) release promotes neurogenic and angiogenic differentiation for enhanced bone regeneration, Bioact. Mater. 25 (2023) 399–414.
[87] X. Wang, L. Pan, A. Zheng, L. Cao, J. Wen, T. Su, X. Zhang, Q. Huang, X. Jiang, Multifunctionalized carbon-fiber-reinforced polyetheretherketone implant for rapid osseointegration under infected environment, Bioact. Mater. 24 (2023) 236–250.
[88] Y. Zhao, J. Li, L. Liu, Y. Wang, Y. Ju, C. Zeng, Z. Lu, D. Xie, J. Guo, Zinc-based tannin-modified composite microparticulate scaffolds with balanced antimicrobial activity and osteogenesis for infected bone defect repair, Adv. Healthcare Mater. 12 (20) (2023) e2300303.
[89] K. Cai, Y. Jiao, Q. Quan, Y. Hao, J. Liu, L. Wu, Improved activity of MC3T3-E1 cells by the exciting piezoelectric BaTiO(3)/TC4 using low-intensity pulsed ultrasound, Bioact. Mater. 6 (11) (2021) 4073–4082.
[90] C. McCarthy, G. Camci-Unal, Low intensity pulsed ultrasound for bone tissue engineering, Micromachines 12 (12) (2021).
[91] Z. Hua, S. Li, Q. Liu, M. Yu, M. Liao, H. Zhang, X. Xiang, Q. Wu, Low-intensity pulsed ultrasound promotes osteogenic potential of iPSC-derived MSCs but fails to simplify the iPSC-EB-MSC differentiation process, Front. Bioeng. Biotechnol. 10 (2022) 841778.
[92] H. Wu, H. Dong, Z. Tang, Y. Chen, Y. Liu, M. Wang, X. Wei, N. Wang, S. Bao, D. Yu, et al., Electrical stimulation of piezoelectric BaTiO3 coated Ti6Al4V scaffolds promotes anti-inflammatory polarization of macrophages and bone repair via MAPK/JNK inhibition and OXPHOS activation, Biomaterials 293 (2023) 121990.
[93] Y. Chen, M. Xiao, L. Zhao, Y. Huang, Y. Lin, T. Xie, J. Tian, Q. Wang, Y. Tang, Z. Su, Low-intensity pulsed ultrasound counteracts advanced glycation end products-induced corpus cavernosal endothelial cell dysfunction via activating mitophagy, Int. J. Mol. Sci. 23 (23) (2022).